

# Light sheet microscopy using an Airy beam

T. Vettenburg,<sup>1</sup> H. I. C. Dalgarno,<sup>1</sup> J. Nylk,<sup>1,2</sup> C. Coll Lladó,<sup>3</sup>  
D. E. K. Ferrier,<sup>3</sup> T. Čížmár,<sup>4</sup> F. J. Gunn-Moore,<sup>2</sup> and K. Dholakia<sup>1</sup>

<sup>1</sup>*School of Physics and Astronomy, University of St. Andrews, St. Andrews, U.K.*

<sup>2</sup>*School of Biology, University of St. Andrews, St. Andrews, U.K.*

<sup>3</sup>*The Scottish Oceans Institute, Gatty Marine Laboratory, School of Biology,  
University of St. Andrews, St. Andrews, U.K.*

<sup>4</sup>*School of Medicine, University of St. Andrews, St. Andrews, U.K.*

*Corresponding authors:*

*T. Vettenburg <tv2@st-andrews.ac.uk> and K. Dholakia <kd1@st-andrews.ac.uk>*

Light sheet microscopy facilitates rapid, high contrast, volumetric imaging with minimal sample exposure. However, the rapid divergence of a traditional Gaussian light sheet restricts the field-of-view that provides innate sub-cellular resolution. We show that the accelerating Airy beam innately yields high contrast and resolution up to a ten-fold larger field-of-view. In contrast to the Bessel beam which also provides an increased field-of-view, the Airy beam's characteristic asymmetric excitation pattern results in all fluorescence contributing positively to the contrast, enabling a step change for light sheet microscopy.

Light sheet microscopy facilitates high contrast, volumetric imaging with minimal sample exposure by using two objectives placed orthogonally to one another that perform the tasks of excitation and detection. The lateral resolution is solely dictated by the numerical aperture (NA) of the detection objective whereas the axial resolution is determined by a combination of the NA of the detection optics and the width of the generated light sheet<sup>1</sup>. To ensure optimal excitation of the sample and isotropic resolution in all three dimensions, there is a simultaneous need for extended, uniformly thin light sheets in the excitation path. The Rayleigh range of the Gaussian beam used in traditional light sheet severely restricts the uniformly illuminated field-of-view (FOV)<sup>2</sup>. Capturing additional exposures of the sample from different angles to increase the FOV, unavoidably leads to a longer irradiation time and may induce photobleaching or damage<sup>3-5</sup>.

Propagation invariant light fields such as Bessel beams can create a thinner light sheet<sup>6</sup> but the transversal outer ring structure of the Bessel beam produces background fluorescence and precludes high axial resolution unless two-photon excitation is used<sup>7,8</sup>. Single photon Bessel beam approaches can reclaim contrast using structured illumination (SI)<sup>7,9</sup> or confocal scanning (CS)<sup>10</sup> but the transversal structure of the Bessel beam still unnecessarily irradiates the sample (**Supplementary Note 1**).

We show that a single-photon light sheet created by the transversely accelerating asymmetric Airy beam<sup>11</sup> provides a wide FOV in which the transverse beam structure contributes positively to the imaging process with no redundancy. As with the Bessel beam, the Airy light field has a propagation invariant intensity profile and can exhibit 'self-healing'<sup>12,13</sup>. With its curved trajectory and asymmetric extended transverse structure parallel to a relatively weak and broad main lobe, the Airy beam may not appear to be advantageous for light sheet imaging; however, both the curved profile and the side-lobes of the generated light sheet are readily accounted for by a simple and efficient deconvolution. The Airy light sheet method thus lends itself to the efficient use of the captured fluorescence. A single Airy beam light sheet scan yields high contrast and resolution over an extended FOV and provides advantages over either a Gaussian or a Bessel beam light sheet. For the case examined here of similar numerical apertures in the excitation and illumination paths, the Airy beam shows up to a ten-fold and four-fold increase in FOV compared to the single-photon Gaussian and Bessel beam light sheets respectively, whilst sustaining high resolution. It can be implemented by a straightforward modification to existing apparatus.

To compare the different light sheet modes we developed a generic light sheet microscope using a spatial light modulator (SLM) to enable the holographic formation of apertured Gaussian, Bessel, and Airy beams as desired (see Online Methods). A fast scanning acousto-optic deflector (AOD) broadened each of the focused beams along the lateral y-dimension into light sheets within the sample volume (**Fig. 1** and **Supplementary Fig. 1**).

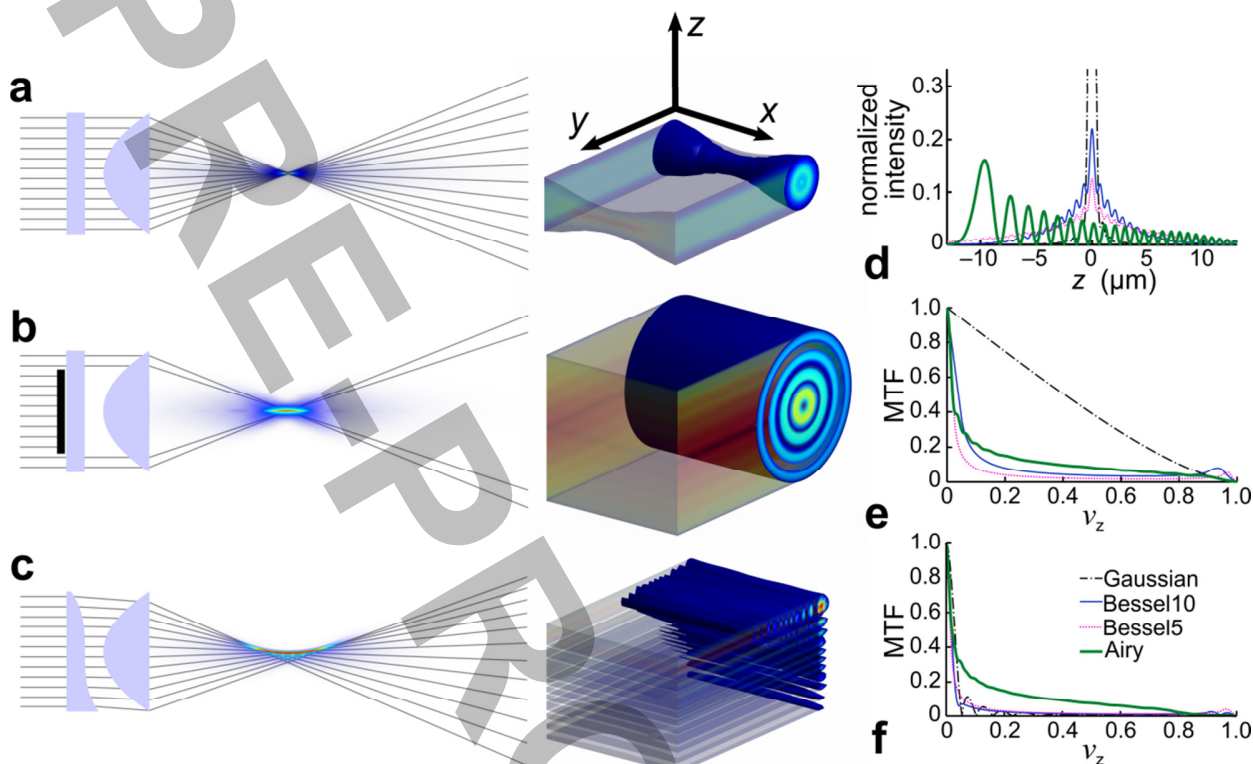


**Figure 1:** Airy beam light sheet microscopy. **(a)** The generation of a conventional apertured Gaussian, **(b)** a Bessel, and **(c)** an Airy profile. Quantitative plots of the transversal light sheet intensity distribution are shown in **(d-f)**. **(d)** The transversal light sheet intensity distribution at the waist of four light sheets created with: an apertured Gaussian beam (dash-dotted black line), Bessel10 (solid blue line), Bessel5 (dotted red line), and an Airy beam (solid green line). The respective  $z$ -axis modulation transfer functions of the light sheets are shown at the waist **(e)** and at the plane  $x \equiv 25 \mu\text{m}$  **(f)**.

We created two Bessel beams using annular apertures with different width such that the propagation invariance distance matched the required FOV (**Supplementary Notes 2 and 3**). We designated the beams Bessel10 and Bessel5, referring to the ratio  $\beta = w/R = 0.10$  and  $0.05$ , respectively where  $R$  is the objective back aperture radius and  $w$  is the annulus width. Bessel10 allowed us to compare the contrast and resolution for a limited FOV; while Bessel5, a closer approximation to the theoretical Bessel beam, enabled us to assess the detrimental impact on contrast and resolution when increasing the FOV by a factor of two.

The intensity cross sections (**Fig. 1d**) of the scanned light sheets all have an identical total  $z$ -integrated irradiance, thus all light sheets could in principle excite the same number of fluorescence photons when ignoring fluorophore saturation and damage. Such harmful side-effects are reduced for the Bessel and Airy beams as their peak irradiance is only a fraction of that of the apertured Gaussian light sheet: 22% for Bessel10, 12% for Bessel5, and 16% for the Airy beam (**Supplementary Note 1**). We compared the photobleaching rate of the different light sheets using time-lapse measurement of fluorescence from the gel-embedded dye Cy3 during repeated scanning and confirmed that the Bessel5 and Airy light sheets had the lowest rates of photobleaching (**Supplementary Note 4**).

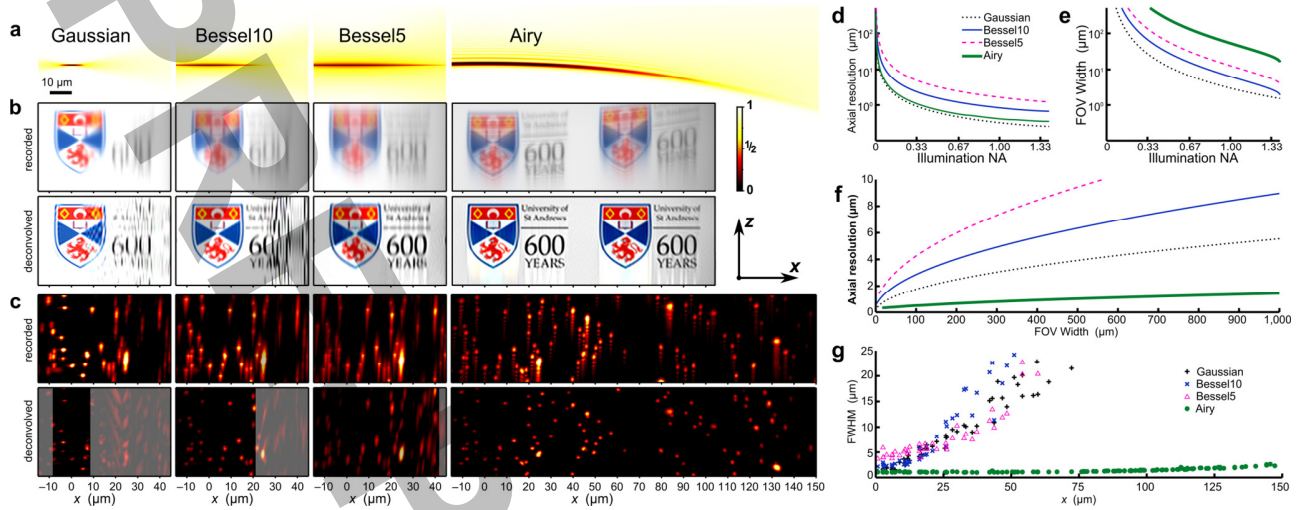


**Figure 2:** Experimental and simulated data for light sheet illumination with various beam types. (a)  $x$ - $z$  section of the light sheet intensity. The light sheets propagate along the  $x$ -axis and are scanned with respect to the sample in the direction of the  $z$ -axis. (b) Light sheet microscopy simulated images of an artificial target closely matching the experimental parameters as specified in the Methods Section (top row) and deconvolution of the simulated images (bottom row). (c) Maximum intensity projections of fluorescent microspheres fixed in PDMS (top row) and deconvolution of the experimental data (bottom row). All images have the same scale and coordinate system in which the illumination focus is situated at  $x = 0$ . False-color coding is used for clarity of the light sheet profiles (inverted) and experimental images. Due to zeros in the MTF, deconvolution artifacts may be seen in the areas outside the theoretical FOV, marked in gray. (d-f) The trade-off between the axial resolution, illumination NA, and field-of-view: (d) the intrinsic axial resolution of the light sheet versus its NA, (e) the field-of-view versus NA, and (f) the axial resolution as a function of field-of-view. The line types used in panels (e) and (f) follow that specified in the legend of panel (d). (g) The experimentally determined full-width-at-half-maximum (FWHM) as a function of the distance from the light sheet waist.

A light sheet image scan can be understood mathematically as a convolution of the light sheet illumination with the fluorophore distribution in the sample. This makes it convenient to study the light sheet illumination process in the spatial frequency domain using the modulation transfer function (MTF), defined as the absolute value of the normalized optical transfer function (**Supplementary Note 5**). The MTF denotes relative image contrast as a function of spatial frequency and provides a valuable insight into the relationship between contrast and resolution of images obtained (**Supplementary Note 3**). Ideal imaging is achieved when the MTF is equal to one for all spatial frequencies. We compared the  $z$ -axis modulation transfer function of the beams at the waist (**Fig. 1e**) and  $25 \mu\text{m}$  distant (**Fig. 1f**). The Gaussian beam had the highest contrast at the waist but this fell rapidly by  $x = 25 \mu\text{m}$ . Although the Bessel and the Airy beams exhibited much lower contrast at the waist they maintained their intensity cross section, and hence contrast, upon propagation. The same image sharpness seen at the light sheet waist will therefore be available over an FOV only limited by the length of the propagation invariant region.

The Bessel5 beam had the lowest contrast and highlights an important trade-off between the distance of propagation invariance and contrast for the Bessel beams (**Supplementary Notes 2 and 3**). Conversely, the MTF associated with the Airy beam maintained high values, even for spatial frequencies close to the diffraction limit. This is a consequence of the asymmetry of the Airy light sheet. Its optical transfer function is a function of both propagation distance and spatial frequency and the ensuing phase shift does not affect the signal-to-noise ratio (SNR). Both the image warping due to the inherent light sheet curvature and the blurring due to its side-lobes can be readily reversed with standard deconvolution techniques. Using simulations we found that an efficient one-dimensional  $z$ -axis deconvolution based on theoretical light sheets (**Fig. 2a**) was sufficient to recover near diffraction-limited resolution (**Fig. 2b** and **Supplementary Note 6**). We anticipate that direct measurement of the light sheet could further improve the deconvolution process.

To experimentally characterize the FOV of all considered light sheets, we imaged a three-dimensional distribution of  $1\ \mu\text{m}$  diameter fluorescent microspheres fixed in poly-dimethylsiloxane (PDMS) within a capillary. With the apertured Gaussian light sheet, the fluorescent microspheres were well resolved within  $8\ \mu\text{m}$  of the beam waist but image contrast degraded rapidly beyond this point. The Bessel5 and Bessel10 light sheets extended the FOV to approximately  $\pm 21\ \mu\text{m}$  and  $\pm 41\ \mu\text{m}$  respectively, coinciding with the decline in the on-axis beam intensity (**Fig. 2a**). In general, the propagation distance of a Bessel beam is increased by reducing  $\beta$  (**Supplementary Note 2**). However, a reduction in  $\beta$  also has an adverse effect on resolution (**Supplementary Note 3**). Extending the FOV by a factor of two, i.e. changing from Bessel10 to Bessel5, resulted in lower axial resolution (**Fig. 2c**). In contrast, the FOV of the Airy beam was an order of magnitude larger than that of the apertured Gaussian beam but maintained comparable resolution; The Airy beam resolution and FOV exceeded those of the two Bessel beams (**Fig. 2c**).

Interestingly, the width of the main lobe of the Airy beam is typically about twice that of the Gaussian light sheet's waist, yet the axial resolution obtained with both light sheets was comparable. This reinforces our view that, in contrast to the outer lobes of the Bessel beam, the side-lobes of the Airy beam contribute positively to the image formation.

Light sheet microscopy can improve the axial resolution of the wide field microscope by restricting the illumination to a width smaller than the depth-of-focus of the detection objective. Both the axial resolution and the field-of-view then depend upon the NA of the illumination objective and the light sheet type. We used simulations to examine the relationship between axial resolution, NA, and field-of-view for the four light sheet types. In all cases there was a trade-off between axial resolution and FOV. Increasing the NA of the illumination objective reduced the light-sheet width, thus increasing axial resolution (**Fig. 2d**), but this decreased the FOV (**Fig. 2e**). However, for most light-sheet types the intrinsic axial resolution is often large (**Fig. 2f**). For this reason, and in contrast to our configuration, it is important to note that a higher NA detection objective is often used to limit the depth-of-field of the detection path and increase axial resolution. The trade-off between axial resolution and FOV is far less severe for the Airy light sheet, where the intrinsic axial resolution remains smaller than  $1.5\ \mu\text{m}$  at the light sheet waist, in theory even for a FOV as wide as 1 mm.

To experimentally compare the resolving power of the different light sheet types we measured the full-width at half maximum (FWHM) of 50 isolated fluorescent microsphere images obtained from the sample shown in **Fig. 2c**. Because the fluorescence detection path in a light sheet microscope is identical to that of a wide-field microscope, similar lateral resolution could be expected but spherical aberrations induced by the air-glass interface of the square capillary resulted in a lateral FWHM of  $1.9\ \mu\text{m} \pm 0.3\ \mu\text{m}$  (std. dev.) for all four light-sheets. We also measured the axial resolution across the FOV (**Fig. 2g**). The FWHM achievable with the Gaussian light sheet was approximately linearly dependent on the distance,  $x$ , from the light sheet waist along the entire FOV. This dependency was reduced for the Bessel beam light sheets up to a distance inversely proportional to  $\beta$ , approximately  $20\ \mu\text{m}$  and  $40\ \mu\text{m}$  for Bessel10 and Bessel5, respectively, after which the FWHM increased rapidly. In comparison, the FWHM obtained with the Airy light sheet increased gradually and remained within  $1.5\ \mu\text{m}$  up to a distance of  $100\ \mu\text{m}$  from the center of the FOV.

We next	Half-FOV ( $\mu\text{m}$ )	Resolution (nm)	Efficiency (%)	Peak Irrad./Efficiency (%)
Gaussian	8	726	99.5	100.0
Bessel10	21	1866	93.9	23.2
Bessel5	41	3883	84.7	14.7
Airy	173	865	74.3	21.6

**Table 1:** Comparison of various scanned light sheet types without post-excitation fluorescence filtering.

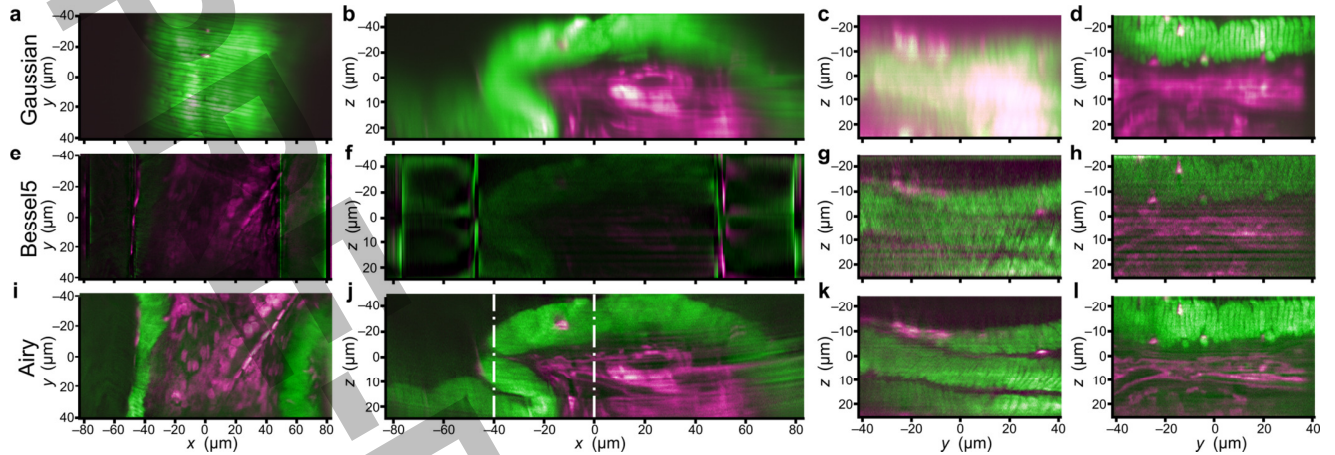


**Figure 3:** Light sheet microscopy scan of a juvenile amphioxus. Volumetric images were acquired using Gaussian (a,b,g-j), Bessel (c,d,k-n) and Airy (e,f,o-r) illumination beams. F-actin is stained using Alexa Fluor 488 Phalloidin (green), and propidium iodide is used as a counterstain indicating nucleic acid material (recolored magenta). Two-dimensional sections are shown at  $z = 0\ \mu\text{m}$  (a,c,e), and at  $y = 0\ \mu\text{m}$  (b,d,f), for the respective beam types. Two sections along the light-sheet propagation axis ( $x$ ) are shown for planes at  $x = -40\ \mu\text{m}$  (c,g,k), and  $x = 0\ \mu\text{m}$  (d,h,l).

The Bessel beam light sheets displayed a lower efficiency due to their broad transverse structure, yet more than 50% of the light could still be captured for a propagation invariant distance of  $103\ \mu\text{m}$ . Relative to the apertured Gaussian light sheet they possessed a reduced peak-irradiance leading to a potential advantage in terms of reduced photobleaching. There was a clear trade-off however between FOV and axial resolution when using a smaller annulus to generate Bessel beams with longer propagation distances.

Two different methods, structured illumination (SI) and confocal scanning (CS), have been described to remove the fluorescence arising from the Bessel beam side lobes, thus mitigating the reduction in axial resolution. For SI the sample is irradiated by multiple beams, and for CS the fluorescence from the outer lobes of the Bessel beam is blocked. A side-effect of these processes is that only a fraction of the excited fluorescence is used for imaging and thus the irradiance of the sample must be increased to achieve a comparable SNR (**Supplementary Note 1**). This increase in irradiation practically nullifies the reduction in peak irradiance. More than 80% of the sample is irradiated unnecessarily when using SI and over 90% of the fluorescence is rejected when using CS. The combination of Airy light sheet illumination and deconvolution discards little fluorescence, allowing sample irradiation to be kept to a minimum. Due to the high efficiency, the peak irradiance can be reduced nearly five-fold.

Further, we assessed the performance of all light sheet types on a variety of biological samples. We first examined membrane-labeled renal adenocarcinoma (ACHN) cells using an equivalent set-up where the objective lenses were both replaced with water-dipping objectives and stopped down to match the numerical apertures of the set-up used to image fluorescent microspheres. The resolution was comparable for both Gaussian and Airy light sheet modes in the lateral dimensions  $x$  and  $y$  (**Supplementary Fig. 2a** and **b**), whereas the axial resolution degraded within  $10\ \mu\text{m}$  of the focus for the Gaussian light sheet while the Airy beam allowed sub-cellular axial resolution for all cells (**Supplementary Fig. 2c** and **d**). For a larger sample the Gaussian focus is affected by cells in the light path (**Supplementary Fig. 3a,e**). Even without *in situ* aberration correction<sup>14,15</sup>, the Airy light sheet can obtain high resolution throughout the  $80\ \mu\text{m}$  FOV (**Supplementary Fig. 3b,d,f**). We believe this may be aided by the relative insensitivity of propagation invariant beams to optical obstacles<sup>13,16</sup>.

As an example of a large, highly scattering sample, we imaged actin and nucleic acid in a juvenile amphioxus (**Fig. 3**), a marine invertebrate. A gradual decrease in image brightness and sharpness was apparent for increasing  $x$  as the light sheet penetrated the sample, and refractive index inhomogeneities precluded a sharp focus of the Gaussian light sheet. In comparison, the Bessel5 beam and Airy beam images displayed increased sharpness of the fiber-structures deep within the organism. The Bessel beam did however show a reduction in contrast and an amplification of the photon noise (**Fig. 3e-h**) as well as image artefacts at both ends of the propagation-invariant region (**Fig. 3e,f**). Visibly higher contrast was observed in the Airy light sheet images (**Fig. 3i-l**). Similarly, imaging of the tail of a juvenile amphioxus stained with propidium iodide using all beam types showed the highly organized

arrangement of nuclei in the notochord, but it was only fully resolved across the whole field-of-view with the Airy beam (**Supplementary Fig. 4**). Finally, only the Airy beam light sheet clearly resolved fine details such as individual sarcomeres in a muscle block of a zebrafish larvae (**Supplementary Fig. 5**).

In contrast to the Bessel beam, the transversal intensity profile of the Airy beam can be exploited to ensure high axial resolution over an extended field-of-view without increasing the sample exposure, or increasing the number of images required. This can be readily achieved by simply introducing a cubic phase mask at an appropriate position in the optical train of a single photon light sheet microscope. The Airy beam light sheet thus presents a powerful advance towards high resolution imaging of large biological specimens with limited sample irradiation.

## **Acknowledgments**

The project was supported by the UK Engineering and Physical Sciences Research Council, RS MacDonald Charitable Trust, Scottish Universities Life Sciences Alliance, and the St. Andrews 600<sup>th</sup> anniversary BRAINS appeal. The PhD apprenticeship of C.C. was funded by the School of Biology. The authors thank A.M. Tilston-Lunel, M.L. Torres-Mapa, Z. Allen, and A. Chatterton for their assistance with the cell culture, M. Ploschner for advice and proofreading of the manuscript, P.A. Reynolds for the fruitful discussions on the biological aspects of this study, and C. Penedo for his assistance with the photobleaching studies.

## **Author contributions**

The Airy beam light sheet was developed by T.V. and K.D. T.V., H.I.C.D., T.Č., and J.N. conducted all the experiments. C.C. and D.E.K.F. provided and prepared the amphioxus and zebrafish samples and assisted with the imaging and interpretation. F.J.G. assisted with all the biological experiments. J.N. and T.V. performed the simulations and data processing. T.V. and K.D. wrote the manuscript with contributions from all the authors.

## Online Methods

### Simulations

The light sheet for each illumination mode is calculated from the corresponding pupil-function as the vectorial point-spread function, and integrating its intensity along the  $y$ -axis. The theoretical light sheet profile is employed both for deconvolution as well as for the simulations shown in **Fig. 2**. The acquisition is simulated as a standard wide-field diffraction-limited detection process with Poissonian distributed noise, corresponding to a charge-coupled device (CCD) array with a well depth of 18,000 electrons. Before simulating the deconvolution, the recorded signal is quantized by an 8-bit analogue-to-digital conversion. The deconvolution procedure itself is detailed in **Supplementary Note 6**.

### Light sheet microscopy setup

The laser beams (Coherent Verdi V6, 6W 532 nm and Spectra Physics Argon-ion 2040E, 10W, 488 nm) are passed through a single mode fiber and expanded to fill the aperture of an acousto-optical deflector (AOD, Neos AOBD 45035-3, see **Supplementary Fig. 1**) which creates the light sheet by scanning the laser focus along the  $y$ -axis. The scan period of 50  $\mu$ s is considerably shorter than the exposure time in our experiments (10ms $\rightarrow$ 50ms). The AOD aperture is re-imaged by a 2 $\times$  magnifying telescope (L1 and L2) to overfill the active area of a spatial light modulator (SLM, Hamamatsu LCOS X10468-04). Instead of a static phase mask, we employed an SLM to enable rapid dynamic switching of the light sheet type. The SLM enabled us to record data sets for the various beam types with the same set-up. The SLM reflects a disk shaped area in the case of the apertured Gaussian and Airy beams. In the case of the Bessel beams the central part of the aperture is blocked and only an annular area is used. The Airy beam is created by modulating the wave front at the back aperture with a cubic polynomial function:  $\alpha(u_y^3 + u_z^3)\lambda$ , where  $u_y$  and  $u_z$ , are the normalized Cartesian pupil coordinates aligned with the  $y$  and  $z$ -axes respectively, and  $\lambda$  is the excitation wavelength. The dimension-less parameter  $\alpha$  dictates the propagation invariance of the Airy beam (**Supplementary Note 2**). Unless otherwise stated, the value of  $\alpha = 7$  was used as it ensures near diffraction-limited resolution across the entire FOV of our experimental set-up (**Supplementary Notes 2 and 3**). Importantly, the use of an SLM also permitted the elimination of residual aberrations in the system<sup>14,15</sup>, thereby ensuring that the beams closely resemble their theoretical descriptions. The active area of the SLM is imaged onto the back aperture of the excitation objective (MO1, Mitutoyo 20 $\times$ /0.42, working distance 20mm, see **Supplementary Fig. 1**), via a demagnifying telescope (0.5 $\times$ ) with a slit aperture at its focus to select the first diffraction order. The sample was mounted on an xyz piezo-stage (Mad City Labs, Nano-LP200) to allow automatic positioning with respect to the light sheet and the focal plane of the detection objective. Depending on the sample and wavelength, the power at the back aperture was set between 30  $\mu$ W and 300  $\mu$ W and kept constant during recording with the different light sheet types. The irradiance of the light sheet for imaging cells was typically 70  $\text{Wcm}^{-2}$ . Fluorescence was detected using a CCD camera (CCD1, Basler piA640-210gm) via an orthogonally mounted objective (MO2, Newport 20 $\times$ /0.40) with an appropriate tube lens (TL1) and fluorescence filter. Beam characterization and alignment are aided by the auxiliary objective (MO3, Mitutoyo 50 $\times$ /0.55), and camera (CCD2, Basler piA640-210gm) with an appropriate tube lens (TL2). A combination of piezo-stage translation and holographic deflection with the SLM was used to scan the fluorescent microsphere sample in 50nm steps, while biological samples were scanned in steps of 200nm. LabVIEW software (National Instruments) was used to interface the camera, nanostage, SLM, AOD, and lasers. An equivalent set-up was used to image biological samples water-immersed in a Petri dish. The objective lenses MO1 and MO2 were both replaced with stopped down water dipping objectives (Nikon CFI Apo 40 $\times$ /0.80 DIC, working distance 3.5 mm) and image stacks were recorded with an sCMOS camera (Orca Flash 4.0, Hamamatsu).

### Measurement of bleaching rate

Homogeneous test samples with a high concentration of Cy3-streptavidin (645 M, Life Technologies) were prepared using 15% polyacrylamide gel and left over night to set and limit the diffusion of the dye through the gel matrix. The fluorescence intensity was recorded as a function of time and position  $x$  in the field-of-view. Photobleaching was seen throughout the field-of-view of the camera; however, the field-of-view of the respective light sheet types (**Supplementary Note 1**) marked the region with the highest rate of photobleaching. The photobleaching rate was determined by integrating the fluorescence intensity over a 10 $\mu$ m wide volumetric section centered at the point with

the highest photobleaching rate. This point was generally located a few micrometers closer to the illumination objective than the light sheet waist, we attribute this to absorption along the propagation axis.

## Cell culture

Renal cell adenocarcinoma (ACHN, CLS Cell Line Services) cells were grown in rotating culture flasks (CELLSPIN, Integra Biosciences) under standard conditions (37°C, 5% CO<sub>2</sub>) and in growth medium comprising Dulbecco's Modified Eagle's Medium (DMEM, Sigma Aldrich) for 2-3 weeks to form spheroids. The cell line was routinely tested for mycoplasma (negative).

## Sample preparation

The plasma membrane of the ACHN cell spheroids was stained with an Alexa Fluor 488 conjugate of Wheat Germ Agglutinin (Alexa Fluor 488 WGA, Life Technologies) following the recommended protocol for labeling pre-fixed eukaryotic cells; the ACHN cell spheroids were fixed with 4% paraformaldehyde (PFA, Sigma Aldrich) and incubated at 37°C for 15 minutes and then washed three times in Hank's Balanced Salt Solution (HBSS, Sigma Aldrich), WGA conjugate was then added at a concentration of 5 g/mL and the mixture incubated for 10 minutes at room temperature, the cells were washed twice with HBSS and finally suspended in HBSS. As the ACHN cell spheroids were in suspension, removal of the PFA, wash and WGA conjugate was performed by gently centrifuging (100×g) to allow the cells to form a pellet and removing the supernatant.

Tissue phantoms were prepared by mixing fluorescent microspheres (1 μm diameter, R0100, Duke Scientific) with liquid polydimethylsiloxane (PDMS, Slygard 184 Elastomer Kit, Dow Corning) and pipetted into a borosilicate square-profile capillary (Vitrotube 8250-100, Hawksley) before curing at 60°C for two hours. Additionally, the fluorescent microspheres were used as calibration probes for *in situ* wavefront correction<sup>14,15</sup>. Note that for imaging of highly turbid samples this method could be combined with the use of a deformable mirror in the detection path as recently demonstrated<sup>17</sup>.

Cell solutions were prepared for suspension by adding a liquid 1% low-melting point agarose solution (peq-GOLD, Peqlab) and gentle mixing. A small 50 μL drop of the mixture was then placed in a Petri dish and allowed to set for ten minutes.

A 17 days-post fertilization zebrafish larvae (*Danio rerio*, gender not determinable at age) was humanely killed by an overdose of ethyl 3-aminobenzoate methanesulphonate (MS-222, Sigma). Schedule 1 techniques are used in compliance with the Animals (Scientific Procedures) Act regulations and are authorised by the Animal Welfare and Ethics Committee of the University of St. Andrews. Both zebrafish and juvenile amphioxus (*Branchiostoma lanceolatum*, gender not determinable at age) were fixed in 4% (m/v) PFA in morpholinopropanesulfonic acid buffer (0.5 M NaCl, 2 mM MgSO<sub>4</sub>, 1 mM EGTA, 0.1 M morpholinopropanesulfonic acid buffer, pH 7.5) for one hour at room temperature and then washed three times in PBT (1x phosphate buffered saline solution, 0.1% Triton X-100). After peeling the amphioxus 'skin' off, both specimens were permeabilized in PBT for one hour at room temperature. Prior to the staining, an RNase treatment was performed, consisting of a brief wash in 2x SSC (0.3 M NaCl, 0.03 M sodium citrate, pH 7.0), followed by incubation with 100 g/mL DNase-free RNase A (Promega) in 2xSSC for 20 minutes at 37°C, and three washes with 2x SSC. Non-specific binding sites were blocked with 5% normal goat serum (NGS), 1.5% bovine serum albumin (BSA), 0.1% Triton-X100 in phosphate buffered saline solution (PBS) for one hour at room temperature. To visualize actin filaments, the specimens were stained overnight at 4°C in continuous agitation, with Alexa Fluor 488 Phalloidin (Life Technologies) diluted 1:40 (v/v) in 1.5% BSA, 0.1% Triton X-100 PBS. After a brief wash in 2x SSC, a 1:1650 (v/v) dilution of propidium iodide (PI, Life Technologies) in 2x SSC was employed as nuclear counterstaining for 15 minutes at room temperature. Samples were rinsed several times in 2x SSC and embedded in 1% low-melting point agarose in a Petri dish.



## References

1. Engelbrecht, C.J. & Stelzer, E.H. *Opt. Lett.* **31**, 1477–1479 (2006).
2. Sheppard, C.J.R. *Opt. Express* **21**, 6339–6345 (2013).
3. Huisken, J. & Stainier, D.Y.R. *Opt. Lett.* **32**, 2608–2610 (2007).
4. Krzic, U., Gunther, S., Saunders, T.E., Streichan, S.J. & Hufnagel, L. *Nat. Methods* **9**, 730–733 (2012).
5. Tomer, R., Khairy, K., Amat, F. & Keller, P.J. *Nat. Methods* **9**, 755–763 (2012).
6. Durnin, J., Miceli, J.J. & Eberly, J.H. *Phys. Rev. Lett.* **58**, 1499–1501 (1987).
7. Planchon, T.A. et al. *Nat. Methods* **8**, 417–423 (2011).
8. Olarte, O.E. et al. *Biomed. Opt. Express* **3**, 1492–1505 (2012).
9. Gao, L. et al. *Cell* **151**, 1370–1385 (2012).
10. Fahrbach, F.O. & Rohrbach, A. *Nat. Methods* **9**, 223–223 (2012).
11. Siviloglou, G.A., Broky, J., Dogariu, A. & Christodoulides, D.N. *Phys. Rev. Lett.* **99**, 213901 (2007).
12. Baumgartl, J., Mazilu, M. & Dholakia, K. *Nature Photon.* **2**, 675–678 (2008).
13. Broky, J., Siviloglou, G.A., Dogariu, A. & Christodoulides, D.N. *Opt. Express* **16**, 12880–12891 (2008).
14. Čížmár, T., Mazilu, M. & Dholakia, K. *Nature* **4**, 388–394 (2010).
15. Dalgarno, H.I.C. et al. *Appl. Phys. Lett.* **100**, 191108 (2012).
16. Fahrbach, F.O., Simon, P. & Rohrbach, A. *Nature Photon.* **4**, 780–785 (2010).
17. Bourgenot, C., Saunter, C.D., Taylor, J.M., Girkin, J.M. & Love, G.D. *Opt. Express* **20**, 13252–13261 (2012).

## Competing Financial Interests

The University Court of the University of St Andrews, U.K. has filed a U.K. patent application on this intellectual property right, which is currently progressing through the international patenting process. International Publication Number: WO 2013/150273 A1, published on 10<sup>th</sup> October 2013.

# Light sheet microscopy using an Airy beam

T. Vettenburg,<sup>1,\*</sup> H. I. C. Dalgarno,<sup>1</sup> J. Nylk,<sup>1,2</sup> C. Coll Lladó,<sup>3</sup>

D. E. K. Ferrier,<sup>3</sup> T. Čížmár,<sup>4</sup> F. J. Gunn-Moore,<sup>2</sup> and K. Dholakia<sup>1,†</sup>

<sup>1</sup>*School of Physics and Astronomy, University of St. Andrews, St. Andrews, U.K.*

<sup>2</sup>*School of Biology, University of St. Andrews, St. Andrews, U.K.*

<sup>3</sup>*The Scottish Oceans Institute, Gatty Marine Laboratory,  
School of Biology, University of St. Andrews, St. Andrews, U.K.*

<sup>4</sup>*School of Medicine, University of St. Andrews, St. Andrews, U.K.*

## Supplementary Information

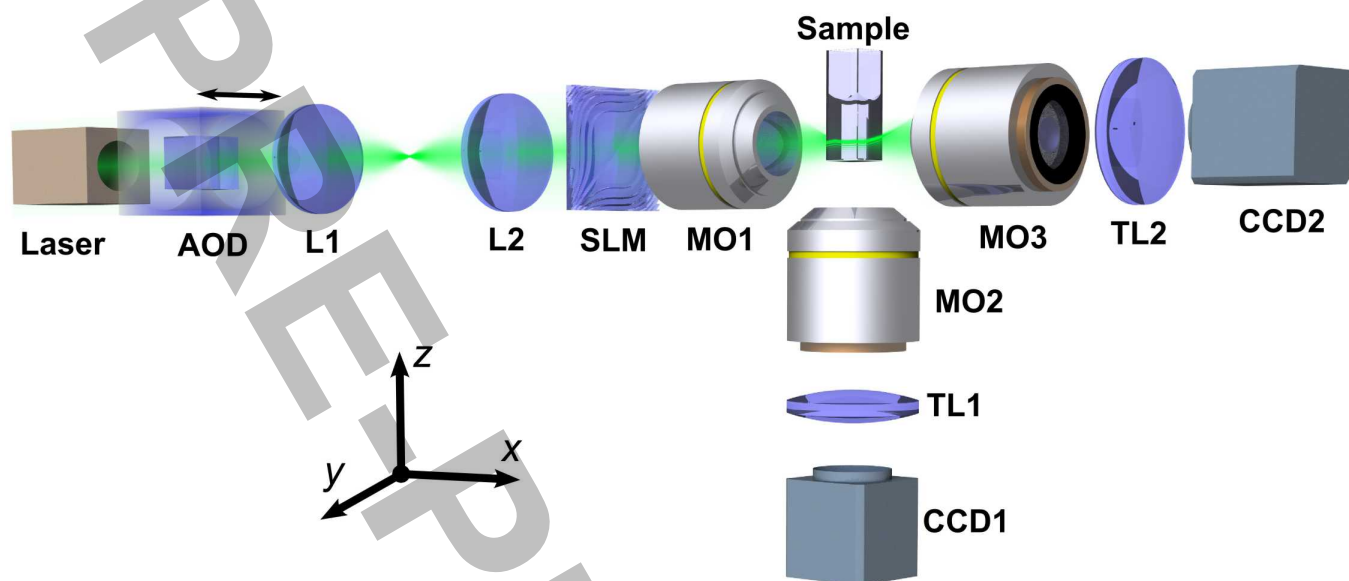
Supplementary File	Title
Supplementary Figure 1	Schematic of the Airy beam light sheet microscope.
Supplementary Figure 2	Lateral and axial projections of a renal adenocarcinoma cell cluster comparing the conventional Gaussian light sheet and the Airy beam light sheet.
Supplementary Figure 3	Axial slice through a 3D volumetric image of an ACHN cell spheroid.
Supplementary Figure 4	Maximum intensity projections of two sections of the tail of a juvenile amphioxus, imaged with the Gaussian, Bessel10, Bessel5, and Airy light sheet.
Supplementary Figure 5	Maximum intensity projections of zebrafish musculature.
Supplementary Note 1	Discussion of the various light-sheet microscopy variants and implementations.
Supplementary Note 2	Field-of-view as a function of the beam parameters.
Supplementary Note 3	Axial resolution as a function of the beam parameters.
Supplementary Note 4	Experimental comparison of the photobleaching rate.
Supplementary Note 5	Modulation transfer function of a light sheet.
Supplementary Note 6	Description of the deconvolution algorithm.

---

\* tv2@st-andrews.ac.uk

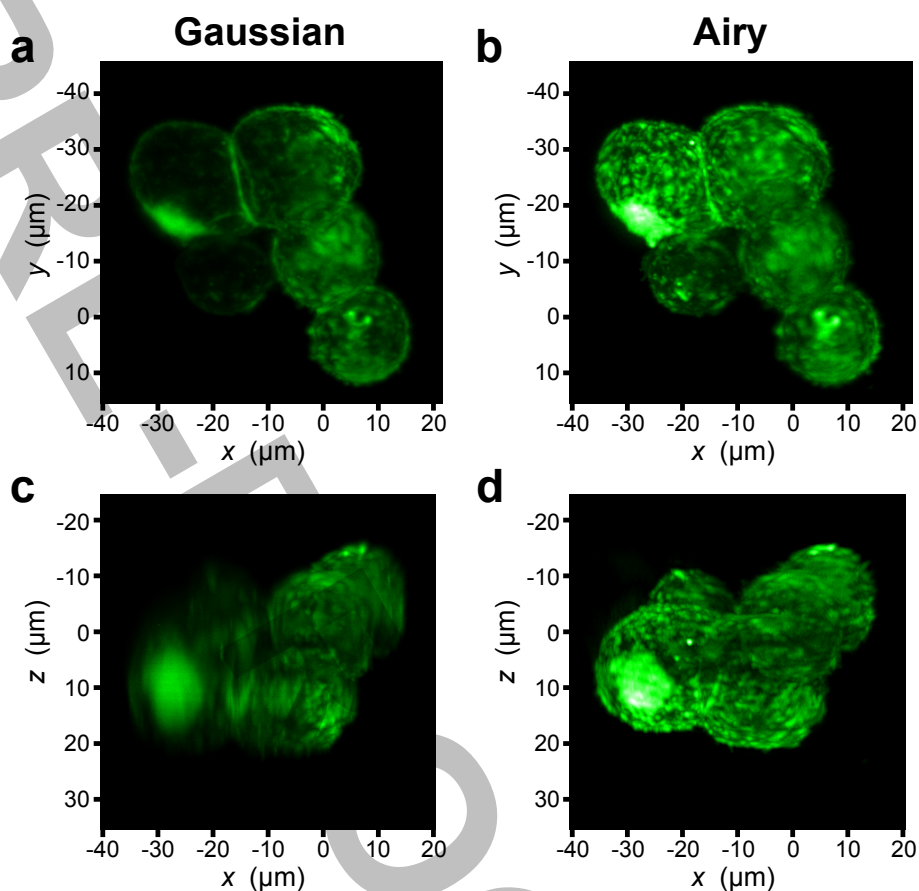
† kd1@st-andrews.ac.uk

## Supplementary Figure 1



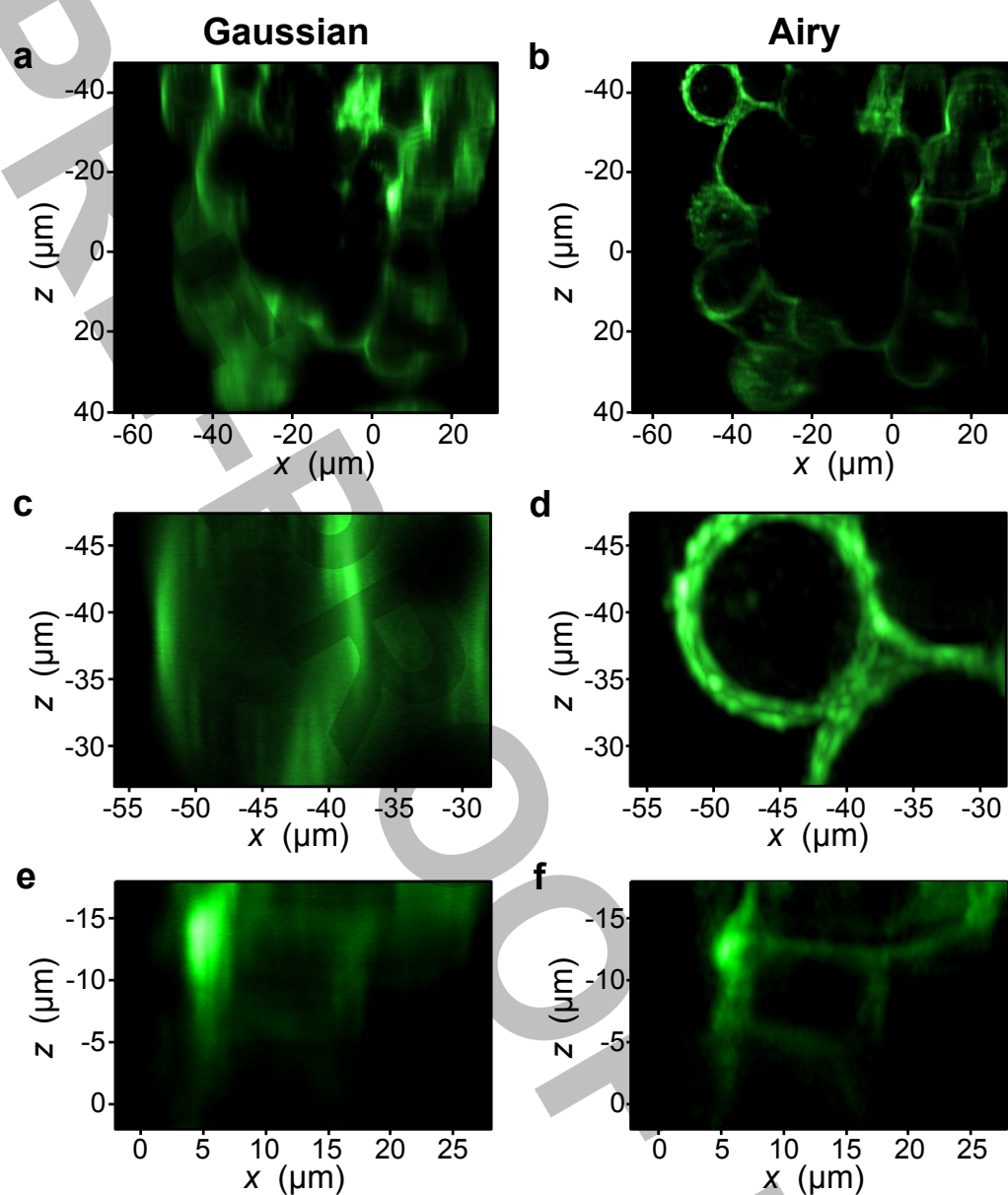
**Supplementary Figure 1.** Schematic of the Airy beam light sheet microscope. The sample (**Sample**) is illuminated with a light sheet emanating from the excitation objective (**MO1**) and propagating along the  $x$ -axis, while the detection objective (**MO2**) and tube lens (**TL1**) collect fluorescence along the  $z$ -axis and form an image on an area detector (**CCD1**). The light sheet is created by expanding coherent light (**Laser**, wavelength  $488\text{ nm}$  or  $532\text{ nm}$ ) to overfill the active area of a fast scanning ( $y$ -axis) acousto-optic deflector (**AOD**) and a spatial light modulator (**SLM**), reimaged using an appropriate telescope (**L1-L2**), and onto the back aperture of the excitation objective (**MO1**, telescope not shown). An auxiliary detection objective (**MO3**), tube lens (**TL2**) and detector (**CCD2**) were used only for the characterization of the light sheet microscope.

## Supplementary Figure 2



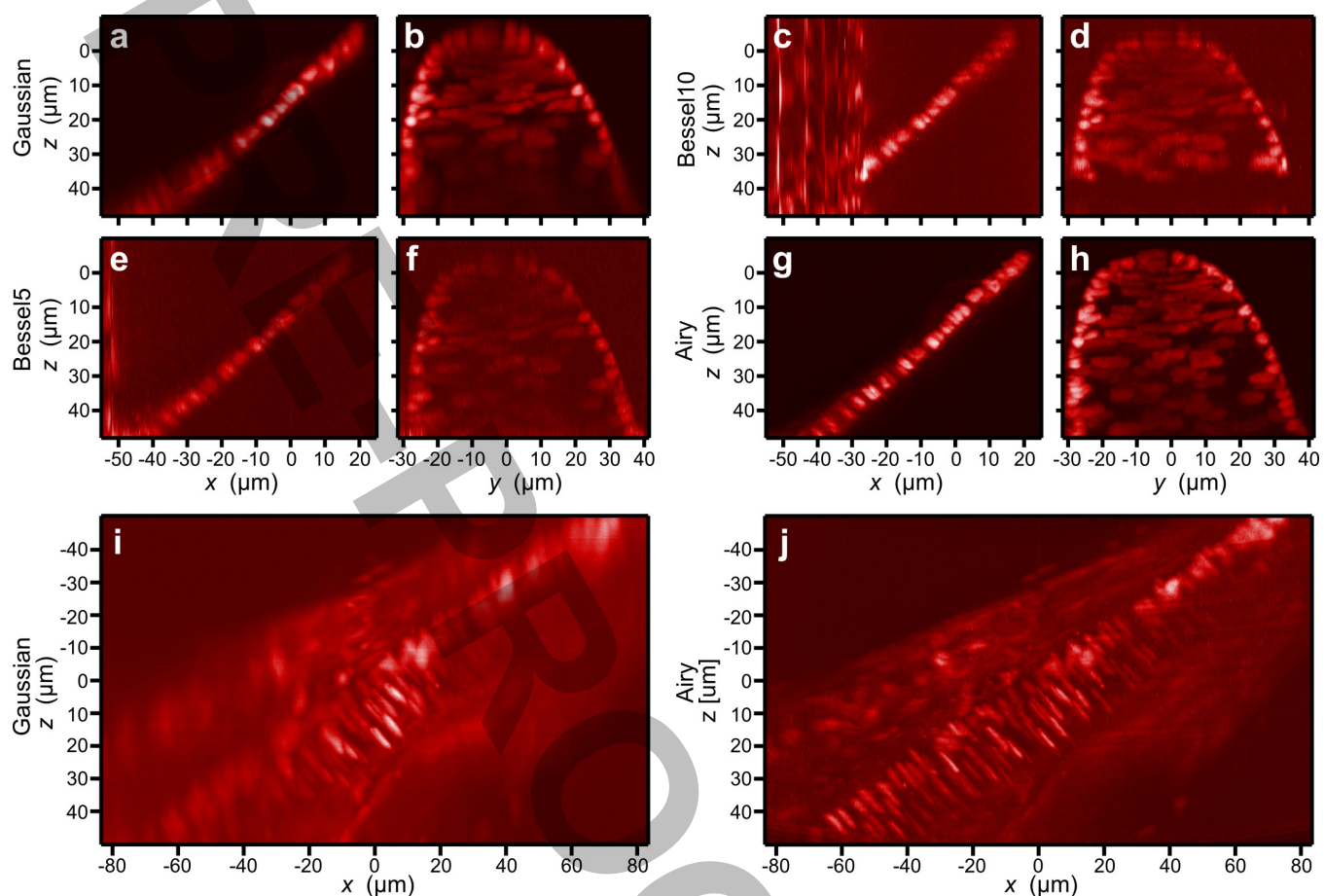
**Supplementary Figure 2.** Lateral and axial projections of a renal adenocarcinoma (ACHN) cell cluster comparing the conventional Gaussian light sheet and the Airy beam light sheet. Maximum intensity projections, along the  $z$  (a,b) and along the  $y$ -axis (c,d), of a cluster of plasma membrane stained (Alexa Fluor 488 WGA) renal adenocarcinoma cells, created by spin culturing the cell line. The same cluster is imaged using the conventional Gaussian light sheet (a,c), and using an Airy light sheet (b,d). Correct deconvolution along the  $z$ -axis is only possible for the volumetric image recorded using the Airy light sheet.

### Supplementary Figure 3



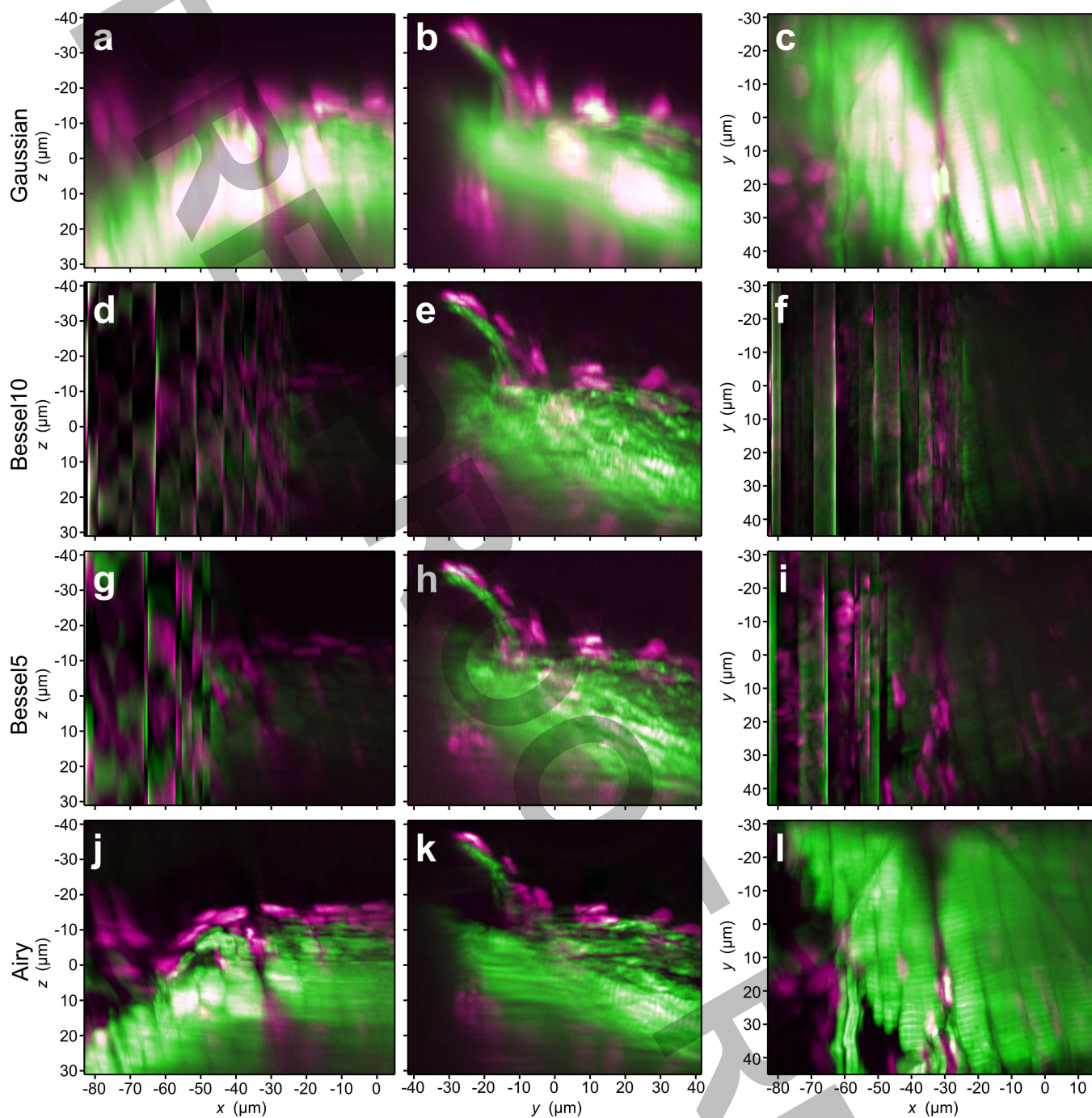
**Supplementary Figure 3.** Axial slice through a 3D volumetric image of an ACHN cell spheroid. The cell spheroid is created by spin culturing a renal adenocarcinoma cell line, where the plasma membranes are stained with Alexa Fluor 488 WGA (see Online Methods). (a) The sample imaged using a conventional Gaussian light sheet. (b) The same sample imaged using the Airy light sheet method. To show a membrane slice far away from the light sheet waist, the  $y$ -position of the slice is chosen so to coincide with the cell membrane in the top left corner. Details of the cell membranes are shown for the conventional Gaussian (c,e), and the Airy light sheet (d,f), near the surface of the cell spheroid (c,d), and through multiple layers of cells (e,f). The cell membrane cannot be resolved without digital processing, and artifacts occur when the conventional light sheet image is deconvolved. The cell membrane can only be resolved well with the Airy light sheet method.

## Supplementary Figure 4



**Supplementary Figure 4.** Maximum intensity projections of two sections of the tail of a juvenile amphioxus, imaged with the different light sheets. Projections along the  $y$ -axis (a,c,e,g) and  $x$ -axis (b,d,f,h) of an amphioxus, stained with propidium iodide, imaged with light sheet microscope using Gaussian (a,b), Bessel10 (c,d), Bessel5, (e,f) and Airy (g,h) beam illumination. In all images the elongated nuclei of the notochord are clearly visible but these are only fully resolved over the entirety of the image using the Airy light sheet method. Additionally, maximum intensity projections along the  $y$ -axis taken in an anterior position of the tail with Gaussian (i) and Airy beam (j) illumination show the notochord (elongated ordered nuclei) and the surrounding muscular tissue. The morphological differences between the notochord and the muscle are only clearly resolved with the Airy light sheet.

## Supplementary Figure 5



**Supplementary Figure 5.** Maximum intensity projections of zebrafish musculature. Projections of  $10\ \mu\text{m}$  thick slices from light sheet image stacks, centered at  $y = 25\ \mu\text{m}$  (a,d,g,j),  $x = -35\ \mu\text{m}$  (b,e,h,k), and  $z = 5\ \mu\text{m}$  (c,f,i,l), acquired using Gaussian (a,b,c), Bessel10 (d,e,f), Bessel5 (g,h,i), and Airy (j,k,l) beam illumination. Images show a section of muscle block within a juvenile zebrafish larva stained with Alexa Fluor 488 Phalloidin (green) to indicate F-actin and propidium iodide (magenta) as a nuclear counterstain. Each color channels (recorded data not saturated) is normalized to its maximum value for visibility and added. The V-shaped intermuscular septa, separating two myomeres, is visible in the  $z$ -axis projection. The dark line at  $x = -30\ \mu\text{m}$  is attributed to the dorsal region of the myotome. Muscle fibers and their sarcomeres can only be clearly resolved in (j,l) and (k,l) respectively, when using the Airy light sheet method.

## Supplementary Note 1: Discussion of the various light-sheet microscopy variants and implementations

In recent years several variants of light sheet microscopy have been developed, often with the aim to improve the axial resolution whilst maintaining a useful field-of-view. Bessel beams have proven useful to illuminate the sample uniformly over the field-of-view. However, without further modification of the conventional light sheet microscope, the fluorescence background from the broad transverse structure of the Bessel beam reduces the axial resolution and contrast. The deteriorating effect of the broad transversal structure of the Bessel beam can be mitigated by relying on two-photon excitation<sup>7</sup>. This technique maintains many advantages of conventional digitally scanned light sheet microscopy, whilst significantly improving the trade-off between axial resolution and field-of-view. However, it depends on the availability of appropriate high power laser sources and fluorescent markers with an adequate two-photon cross-section, thus limiting the ability of multi-color imaging, and the photo-stability of biological samples.

Single photon excitation Bessel beam light sheet microscopy cannot, in principle, achieve high axial resolution. Although in this paper we investigate such propagation invariant modes for the single photon case without additional post-excitation filtering, it should be noted that methods exist that borrow concepts from either structured illumination microscopy (SI) or from confocal scanning microscopy (CS) to separate the fluorescence excited at the focal plane from that excited by the side lobes:

**SI: Bessel beam Light Sheet Microscopy with Structured Illumination:** In this method the sample is not illuminated with an orthogonal plane but with a periodic grid of Bessel beams. By translating the periodic pattern along the  $y$ -axis in the plane of the light sheet, preferentially the fluorescence at the Bessel beam core is modulated. The acquisition of an image sequence allows the computation of an image with an axial resolution comparable to the core of the Bessel beam. Although the acquisition speed is reduced by a small factor, the advantage of high axial resolution over a wide field-of-view makes this an attractive method. Note however that the sample has to be irradiated multiple times per plane, and that even if only fluorescence from the Bessel beam core is used, the whole transversal structure of the Bessel beam unnecessarily irradiates the sample<sup>7,9</sup>.

**CS: Confocal Scanning Light Sheet Microscopy:** A hybrid between light sheet and confocal microscopy can be employed to selectively detect the fluorescence from the central maximum of the Bessel beam. Instead of scanning a spot and filtering the fluorescence with a pinhole as in confocal microscopy, a Bessel beam is scanned while a line detector preferentially detects the light emitted from fluorophores excited by the Bessel beam core<sup>18</sup>. In contrast to a one-dimensional light sheet scan along the  $z$ -axis, a Bessel beam is thus raster-scanned along both the  $y$ - and the  $z$ -axis, and the 3D image will thus be constructed line-by-line instead of plane-by-plane. Although this would require a 2D scan to obtain a 3D image, technological advances could overcome a decrease in acquisition speed. It should however be noted that most of the energy of the Bessel beam is carried in its transversal structure and the associated fluorescence therefore discarded, so part of the sample is irradiated unnecessarily.

As with the Airy beam light sheet method, the Bessel beam methods irradiate the sample with a relatively large transverse structure. Structured illumination or confocal scanning of the Bessel beam can reclaim axial resolution by selectively rejecting fluorescence excited by its transverse structure. However, in this process the sample is still exposed to the photobleaching and potentially damaging irradiation of the transverse structure. In contrast, no fluorescence has to be rejected for the Airy beam method. The deconvolution step recombines all collected fluorescence into a high resolution volumetric image. In practice, fluorescence emitted far from the focal plane cannot be collected efficiently, so no method will be able to utilize all fluorescence emitted within the cone of acceptance of the detection objective.

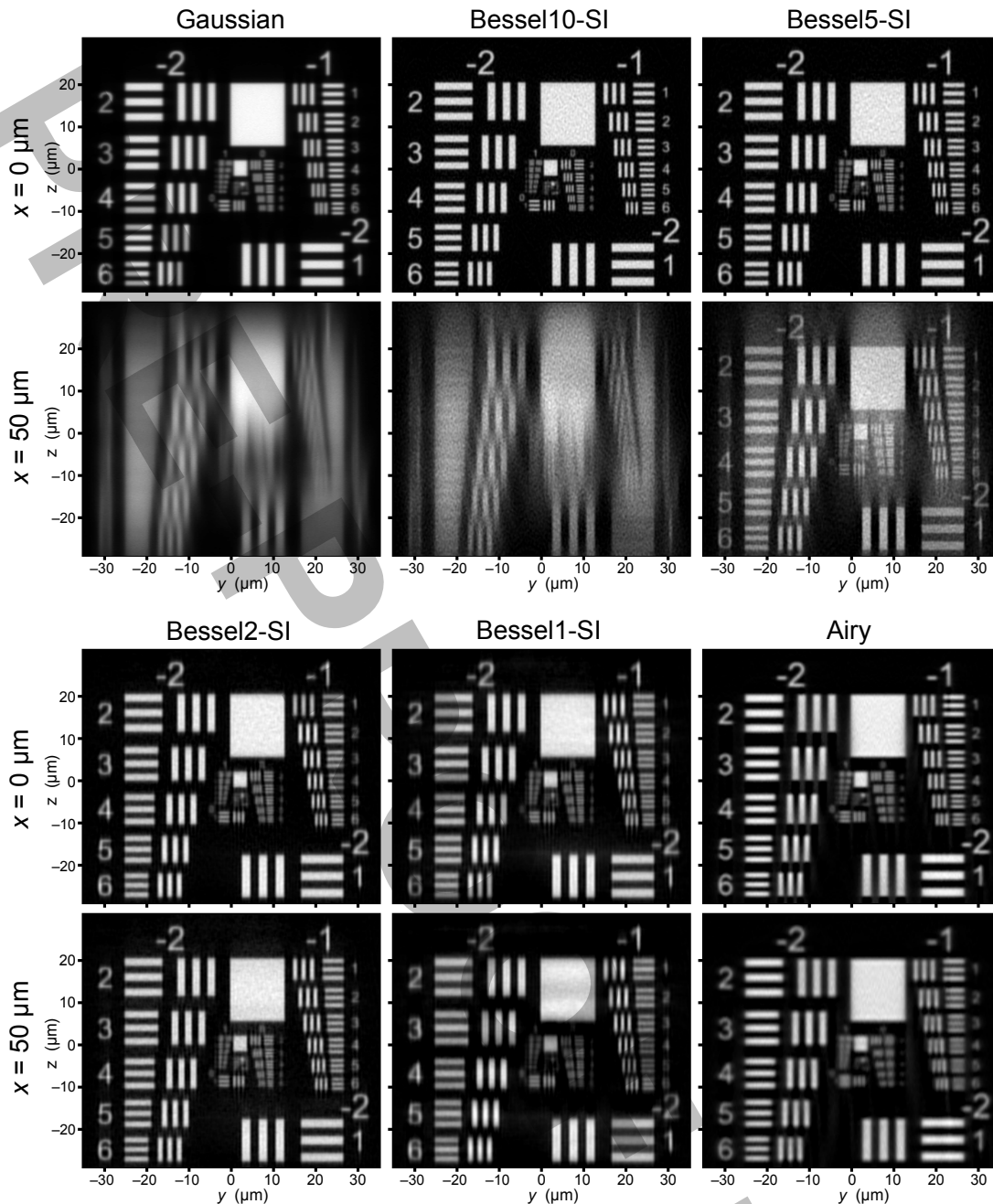
**Supplementary Table S1** shows a comparison of the light sheet microscopy types and variants: the conventional light sheet (Gaussian), Bessel beam light sheets (Bessel10, Bessel5, Bessel2, and Bessel1) where the number indicates the width of the annular aperture as a percentage ratio of the total aperture radius, and Airy beam light sheet (Airy). The post-fix 'SI' refers to the use of structured illumination to isolate the fluorescence excited at a plane with thickness comparable to the Bessel beam core of the corresponding numerical aperture and wavelength. The post-fix 'CS' refers to the use of confocal scanning Bessel beam light sheet microscopy to isolate the core of the Bessel beam, thus also eliminating the fluorescence of transversal structure that falls within the focal plane. The theoretical propagation invariance of all light sheets is given as calculated in **Supplementary Note 2**, followed by the resolution calculated numerically using the criterion in **Supplementary Note 3**, or the smaller core width of the Bessel beam (970 nm) in case of the structured illumination and confocal adaptation (**Supplementary Note 1**). The next column shows the efficiency calculated as the fraction of fluorescence, emitted within the cone of acceptance of the detection objective, that is used to form the final volumetric image. The final column shows the peak irradiance with respect to that of the apertured Gaussian light sheet and for an equal number of used photons.



<i>Type</i>	<i>Half-FOV ( <math>\mu\text{m}</math> )</i>	<i>Axial Res. (nm)</i>	<i>Efficiency (%)</i>	<i>Peak Irrad./Efficiency (%)</i>
<b>Without post-excitation fluorescence filtering</b>				
<b>Gaussian</b>	8	726	99.5	100.0
<b>Bessel10</b>	21	1866	93.9	23.2
<b>Bessel5</b>	41	3883	84.7	14.7
<b>Bessel2</b>	103	8336	57.8	10.5
<b>Bessel1</b>	206	18756	38.8	8.8
<b>Airy</b>	173	865	74.3	21.6
<b>Fluorescence filtering by Structured Illumination (SI) Bessel beam</b>				
<b>Bessel10-SI</b>	21	970	19.5	111.7
<b>Bessel5-SI</b>	41	970	11.6	107.4
<b>Bessel2-SI</b>	103	970	5.9	102.8
<b>Bessel1-SI</b>	206	970	3.4	101.7
<b>Fluorescence filtering by Confocal Scanning (CS) Bessel beam</b>				
<b>Bessel10-CS</b>	21	970	8.2	264.6
<b>Bessel5-CS</b>	41	970	4.1	304.8
<b>Bessel2-CS</b>	103	970	1.7	357.7
<b>Bessel1-CS</b>	206	970	0.9	384.0

**Supplementary Table S1.** Comparison of various types of light sheet microscopy.

Although Bessel beam illumination may not allow optimal use of the photon budget, structured Bessel beam light sheet illumination in combination with three-dimensional super-resolution image-restoration can increase the lateral ( $y$ ) and axial ( $z$ ) resolution beyond the diffraction limit<sup>19</sup>. To limit photo-damage due to high peak powers, instead of stepping a single Bessel beam to form the structured illumination, the same can be achieved with several, e.g. 7, parallel Bessel beams with proportionally lower peak intensity<sup>9</sup>. Ignoring the total sample irradiation, **Supplementary Fig. S1** shows image sections of a fluorescent USAF1951 test target, extended along the light sheet propagation axis ( $x$ ), obtained by simulation of conventional Gaussian, super-resolution structured illumination Bessel beam ( $\beta = 0.10, 0.05, 0.02, \text{ or } 0.01$ ), and Airy beam ( $\alpha = 4$ , see Online Methods) light sheet microscopy. The structured illumination light sheets were formed by stepping the beam with steps of  $1 \mu\text{m}$ , offset by three different phases per  $z$ -slice. Lateral-axial ( $y - z$ ) sections are shown at the light sheet waist ( $x = 0$ ), and at  $x = 50 \mu\text{m}$ . Detector pixelation and photon noise are simulated matching the experimental conditions as described in the Online Methods. The image stacks obtained with the Bessel light sheet are further processed using the three-dimensional structured illumination super resolution algorithm<sup>19</sup>. The Airy light sheet image stacks are simply axially deconvolved with a one-dimensional Wiener filter<sup>20</sup>. The dimensions of the largest bars at the bottom right are  $10 \mu\text{m} \times 2 \mu\text{m}$  and the three bars are separated by  $2 \mu\text{m}$ . Consecutive sets of bars are scaled by  $\sqrt[3]{2}$  so that the set on the top right has bars of size  $5 \mu\text{m} \times 1 \mu\text{m}$ . The intensity of each light sheet type has been adjusted so that, before simulating photon noise, the maximum value on the detector is 80% of the maximum read-out. The intensity reduction along the propagation axis of the Bessel precludes high contrast for Bessel10-SI and Bessel5-SI at  $x = 50 \mu\text{m}$ . Note that the image intensity is renormalized for clarity of display. The transversal structures of Bessel2 and Bessel1 irradiate a relatively wide sample volume; however, structured illumination super resolution can reclaim contrast and resolution at  $x = 50 \mu\text{m}$  due to the larger propagation invariance. Although the Airy light sheet in simple scanning mode cannot quite resolve the same detail as the super-resolution structured illumination Bessel method, it achieves a large field-of-view with near diffraction-limited resolution whilst keeping the sample irradiation to a minimum and below that for the Bessel SR-SIM cases considered. In the example of the images shown in **Supplementary Fig. S1**, the total sample irradiance with respect to the conventional Gaussian light sheet was 3.1, 3.7, 5.5, and 6.6 times higher for Bessel10-SI, Bessel5-SI, Bessel2-SI, and Bessel1-SI, respectively. This increased irradiation is partially due to the multiple acquisitions acquired per frame, one for each of the three phases, and partially due to the broad transversal structure of the Bessel beam for small values of  $\beta$ . In contrast, the Airy light sheet requires only a single sample exposure per  $z$ -slice, in this



**Supplementary Figure S1.** Comparison of conventional, structured illumination Bessel beam, and Airy beam light sheet microscopy. Lateral-axial ( $y - z$ ) sections of a simulated USAF1951 test target, elongated along the light sheet propagation axis ( $x$ ), are shown at the light sheet waist ( $x = 0$ ), and at  $x = 50 \mu\text{m}$ . The sample irradiation was adjusted for each light sheet type so that the maximum fluorescence signal per frame is 80% of the detector saturation. The total irradiance with respect to the Gaussian light sheet was 3.1, 3.7, 5.5, 6.6, and 1.02 times for Bessel10-SI, Bessel5-SI, Bessel2-SI, Bessel1-SI, and the Airy light sheet, respectively. Detector pixelation and photon noise are simulated matching the experimental conditions as described in the Online Methods. The image stacks obtained with the Bessel light sheet are further processed using the three-dimensional structured illumination super resolution algorithm<sup>19</sup>, while the Airy light sheet image stacks are only axially deconvolved with a one-dimensional Wiener filter<sup>20</sup>. More details can be found in Supplementary Note 6. The final image intensity is renormalized for clarity of display. The dimensions of the largest bars at the bottom right are  $10 \mu\text{m} \times 2 \mu\text{m}$ . See note 1 for more information.

case with a total irradiance increase of 2% over that of the conventional Gaussian light sheet. Also the peak-irradiance of the stepped Bessel beam light sheet is significantly higher than that of the conventional light sheet. However, the

use of a diffractive grating can reduce the peak irradiance, e.g. by a factor of seven<sup>9</sup>. Even so, the peak irradiance remains higher than that of a conventional light sheet created by a cylindrical lens, respectively by a factor of 4.1, 2.7, 1.9, and 1.6 for the considered beam types. As the conventional light sheet, the Airy light sheet can be formed by a cylindrical lens. Instead of an increased peak irradiance due to scanning of the beam, the lateral intensity distribution of the Airy light sheet allows a peak irradiance reduction by approximately a factor of five with respect to the Gaussian light sheet, as already suggested by **Supplementary Table S1**.

It should be noted that the Airy light sheet could also benefit from various of the innovations of the Bessel beam super-resolution structured illumination approach. Albeit slower, more complex image restoration algorithms such as three-dimensional deconvolution and in particular iterative algorithms that allow a spatially variant point spread function could further improve the final image quality and reduce restoration artefacts near sharp edges in intensity. Furthermore, the peak intensity of the Airy light sheet illumination needed could be further reduced by a factor creating multiple parallel Airy beams, or even several orders of magnitude by using it in combination with a cylindrical lens. A detailed discussion is outside the scope of this paper.

## Supplementary Note 2: Field-of-view as a function of the beam parameters

In this note we determine the relationship between the field-of-view (FOV) and the pupil function parameters associated with different light sheet types. The FOV obtainable with the traditional apertured Gaussian light sheet,  $FOV_G$ , can be estimated from the axial extent of the diffraction-limited focal spot, which first intensity minimum from the beam waist is found at  $x \approx 2\lambda n/NA^2$ . The FOV can thus be estimated as:

$$FOV_G = 2x \approx 4 \frac{\lambda n}{NA^2} \approx 4 \frac{0.532 \times 1.4}{0.42^2} \mu\text{m} = 17 \mu\text{m}. \quad (1)$$

This inverse dependency on  $NA^2$  emphasizes the trade-off between axial resolution and the FOV of a light sheet microscope.

### The field-of-view of the Bessel beam

In principle, the pupil function of the Bessel beam is an infinitesimally narrow annulus, and the associated intensity profile in the far field is propagation invariant over an infinite FOV. In practice the Bessel beam is often created using Durnin's experimental setup<sup>6</sup>, which has a finite annulus width ( $\beta$ ) to ensure sufficient light transmission. Practical realizations of the Bessel beam remain propagation invariant over a relatively large, yet finite, distance. Note that a comparable restriction exists when employing an axicon to create the Bessel beam. The axicon produces an annular intensity distribution in the far field whereby the annulus width is determined by diffraction effects.

The Bessel beam propagates along the  $x$ -axis and its intensity profile can be written in the paraxial approximation as:

$$I(r; x) \propto |\mathcal{F}\{P(u_r; d)\}|^2, \quad (2)$$

where  $r = \sqrt{y^2 + z^2}$ ,  $u_r$  is the normalized radial pupil coordinate,  $\mathcal{F}\{\cdot\}$  denotes the Fourier transform, and  $P(u_r; d)$  is the pupil function incorporating defocus as a quadratic phase change with magnitude  $d$ :

$$P(u_r; d) = H(1 - u_r)H(u_r - 1 + \beta) \exp(-2\pi i d u_r^2), \quad (3)$$

where  $H(\cdot)$  denotes the Heaviside step function, and  $i$  is the imaginary unit. The amount of defocus,  $d$ , is specified in units of wavelength and is related to the distance,  $x$ , from the focal plane. When  $|x|$  is negligible compared to the focal length, the amount of defocus can be approximated as:

$$d = x \frac{n}{\lambda} \left(1 - \sqrt{1 - (NA/n)^2}\right) \approx \frac{x NA^2}{\lambda 2n}, \quad (4)$$

where  $n$  is the refractive index of the sample,  $\lambda$  is the illumination wavelength, and  $NA$  is the numerical aperture of the illumination objective.

The phase difference  $\Delta\phi$  between the inner and outer edges of the annulus is proportional to the defocus,  $d$ , and also approximately proportional to  $\beta$  for  $\beta \rightarrow 0$ :

$$\Delta\phi = 2\pi d(1 - (1 - \beta)^2) = 2\pi d\beta(2 - \beta) \approx 4\pi d\beta. \quad (5)$$

Destructive interference will occur at the Bessel beam core for  $\Delta\phi > \pi$ . We can estimate the extent of the FOV of the Bessel beam,  $FOV_B$ , as the maximum range over which no destructive interference occurs by combining equations (4) and (5):

$$4\pi x \frac{n}{\lambda} \left(1 - \sqrt{1 - (NA/n)^2}\right) \beta \lesssim \pi \quad (6)$$

$$FOV_B \approx \frac{\lambda/n}{2 \left(1 - \sqrt{1 - (NA/n)^2}\right) \beta} \approx \frac{532/1.4}{2 \left(1 - \sqrt{1 - (0.42/1.4)^2}\right) \beta} \text{ nm} \approx \frac{4.125 \mu\text{m}}{\beta}. \quad (7)$$

It is thus inversely proportional to the width of the annular aperture,  $\beta$ . The Bessel10 light sheet is thus expected to have an FOV of 41  $\mu\text{m}$  and that of Bessel5 will be twice that: 82  $\mu\text{m}$ .

## The field-of-view of the Airy beam

It is well known that the core of the Airy beam is not stationary but rather lies on a parabolic curve<sup>21,22</sup>. An alternative method is therefore used to study the relationship between the parameters of the Airy light sheet and the FOV.

Although alternative approaches have been proposed recently<sup>23,24</sup>, the Airy beam is typically produced via the Fourier transform of a cubic phase modulation of the form  $2\pi\alpha(u_y^3 + u_z^3)$ . As for the Bessel beam, we can incorporate the defocus in the pupil function of the Airy beam:

$$P(u_y, u_z; d) = H(1 - u_r) \exp[2\pi i\alpha(u_y^3 + u_z^3)] \exp(-2\pi i d u_r^2). \quad (8)$$

It is noted that the quadratic phase shift of the defocus can be eliminated with a change in origin in the pupil plane:

$$u'_y = u_y - d/3\alpha \quad (9)$$

$$\alpha u_y^3 - d u_y^2 = \alpha(u'_y + d/3\alpha)^3 - d(u'_y + d/3\alpha)^2 \quad (10)$$

$$= \alpha u_y'^3 + [\alpha 3(d/3\alpha)^2 - 2d^2/3\alpha] u'_y + \alpha(d/3\alpha)^3 - d(d/3\alpha)^2 \quad (11)$$

and equivalently for the  $u_z$ -axis. The last two terms cause a constant phase shift, and therefore have no influence on the intensity distribution. The term  $[\alpha 3(d/3\alpha)^2 - 2d^2/3\alpha] u'_y$  corresponds to a wavefront tilt, causing a shift of the intensity distribution proportional to  $d^2/3\alpha$ . The quadratic dependence on the defocus parameter,  $d$ , is consistent with the well-known concept of accelerating Airy wave-packet propagation.

The far field diffraction pattern depends mainly on pupil values near the origin,  $(u'_x, u'_y) \equiv (0, 0)$ . Elsewhere, rapid changes in the pupil phase will cancel out due to destructive interference. Since the origin translates proportional to the defocus,  $d$ , the intensity profile of the Airy beam is expected to degrade when the stationary point is shifted outside the pupil edge. The FOV can thus be defined as the region in which the stationary point resides within the unity-radius pupil, i.e. for  $d < 3\alpha$ . Substitution of equation (4) results in the following expression for the FOV of the Airy light sheet:

$$\begin{aligned} FOV_A = 2x &= \frac{6\alpha\lambda/n}{1 - \sqrt{1 - (NA/n)^2}} \\ &= \alpha \frac{6 \times 0.532/1.4}{1 - \sqrt{1 - (0.42/1.4)^2}} \mu\text{m} \approx 49 \mu\text{m} \times \alpha \end{aligned} \quad (12)$$

The FOV is thus proportional to the parameter  $\alpha$ , and the experimental parameters  $\alpha = 7$  is expected to yield a FOV of  $343 \mu\text{m}$ . It should be stressed that due to the different approximations, no quantitative comparison of the FOV is possible using equations (7) and (12). However, our experiments confirm that the FOV obtainable with this Airy beam covers the FOV of the detector array, is considerable larger than that of the Bessel beams, and is more than an order of magnitude larger than that of the Gaussian light sheet.

## Supplementary Note 3: Axial resolution as a function of the beam parameters

Aided by digital deconvolution, diffraction-limited resolution can in principle be obtained for any type of light sheet and over an infinite FOV. However, the practically achievable resolution is not only determined by the NA of the light sheet but also by the signal-to-noise ratio (SNR) of the imaging process. As the MTF is proportional to the signal it provides valuable information about the practically achievable resolution. Here we use the MTF to study the practical resolution obtainable with Bessel and Airy light sheet microscopy.

The modulation transfer function (MTF) corresponding to an apertured Gaussian light sheet,  $MTF_G(\nu_z)$ , is well known and given by<sup>25</sup>:

$$MTF_G(\nu_z) = \frac{2}{\pi} \left( \arccos(\nu_z) - \nu_z \sqrt{1 - \nu_z^2} \right). \quad (13)$$

Its MTF decreases monotonically and reaches a 5% threshold at  $\nu_z = 0.88$ . The practical resolution of the apertured Gaussian light sheet,  $r_G$ , can thus be calculated as

$$\begin{aligned} r_G &= \frac{\lambda}{2 \cdot NA \cdot \nu_z} \\ &= \frac{\lambda}{2 \cdot NA \cdot 0.88} = \frac{532 \text{ nm}}{2 \cdot 0.42 \cdot 0.88} = 720 \text{ nm} \end{aligned} \quad (14)$$

### Axial resolution achievable with the Bessel beam

The annulus of the Bessel beam pupil must have a finite width so that sufficient light is transmitted. We will show here that a sufficiently wide annulus is also required to guarantee an acceptable image contrast.

In the Fourier optics approximation, the MTF of the Bessel beam,  $MTF_B(\nu_z)$ , can be calculated from the autocorrelation of the pupil function. At the focal plane, the pupil function of the Bessel beam with unity intensity is given by

$$P_B(u_r) = \frac{H(1 - u_r)H(u_r - 1 + \beta)}{\sqrt{(2\beta - \beta^2)\pi}}. \quad (15)$$

For mid-range spatial frequencies  $\nu_z$ :  $\beta/2 < \nu_z < 1 - \beta$ , the MTF can be approximated using geometrical means as

$$MTF_B(\nu_z) \approx \frac{2}{\pi\beta(2 - \beta)} \frac{\beta^2}{2\nu_z\sqrt{1 - \nu_z^2}} = \frac{\beta}{\nu_z\pi\sqrt{1 - \nu_z^2}(2 - \beta)}. \quad (16)$$

For most spatial frequencies the contrast provided by the Bessel beam light sheet is approximately proportional to the aperture annulus width,  $\beta$ , and decreases with spatial frequency. Unavoidably, the SNR will drop below a level that can be considered useful for experiments. The SNR is proportional to the MTF, yet it also depends on the characteristics of the measurement and the sample. It can be calculated that  $MTF_B(\nu_z)$  will drop below the 5% threshold at  $\nu_z = 0.36$  and  $\nu_z = 0.17$  for the Bessel10 and the Bessel5 light sheet, respectively.

The practical resolution that can be obtained with these Bessel beam light sheets is thus:

$$r_B = \frac{532 \text{ nm}}{2 \cdot 0.42 \cdot \nu_z} = 1.759 \text{ } \mu\text{m} \text{ and } 3.725 \text{ } \mu\text{m}, \text{ respectively.}$$

A linear approximation in  $\nu_z$  of the denominator in equation (16) permits the deduction of an approximate relationship between resolution (equation (15)) and the annulus width,  $\beta$ .

$$MTF_B(\nu_z) \approx \frac{\beta}{(2 - \beta)\pi\nu_z} \quad (17)$$

$$\begin{aligned} r_B &\approx \frac{\lambda}{2NA} \frac{(2 - \beta)\pi 0.05}{\beta} \\ &\approx \frac{\lambda\pi 0.05}{NA\beta} \approx \frac{200 \text{ nm}}{\beta} \end{aligned} \quad (18)$$

By combining equations (7) and (18) it can be seen that the smallest resolvable detail is approximately proportional to the FOV of the Bessel beam light sheet:

$$r_B \approx \frac{FOV_B}{20.6} \quad (19)$$

For optimal contrast and for resolution it is therefore important to ensure that the annulus width,  $\beta$ , is no smaller than that required for imaging a given FOV.

## The axial resolution achievable with the Airy beam

The MTF of the Airy beam,  $MTF_A(\nu_z)$ , can be determined via the autocorrelation of the normalized cubic phase mask pupil,  $P_A(u_y, u_z)$ :

$$P_A(u_y, u_z) = \frac{H(1 - u_r)}{\sqrt{\pi}} \exp(2\pi i \alpha (u_y^3 + u_z^3)). \quad (20)$$

This integrand is highly oscillatory for large values of  $\alpha$  and can be calculated using the stationary phase approximation<sup>26</sup>, as

$$MTF_A(\nu_z) = \frac{1}{\sqrt{48 |\alpha \nu_z|}}, \quad (21)$$

Note that for  $\nu_z \rightarrow 0$  and  $\nu_z \rightarrow 1$  the stationary phase approximation is not valid and  $MTF_G(\nu_z)$  is more accurate.

The MTF approximation decreases monotonically and it can be seen that the Airy light sheet will yield diffraction-limited resolution for values of  $\alpha < 8.33$ . Large values of  $\alpha$  would lead to a gradual reduction in resolution, albeit still with a more favorable trade-off compared to the Bessel beam light sheet. Moderate values of  $\alpha$  are however adequate. We verify numerically that for the value of  $\alpha = 7$ , which already permits more than an order of magnitude extension of the FOV, an axial resolution comparable to the diffraction limit is possible.

Both the axial resolution and the field-of-view depend upon the numerical aperture of the illumination objective and the light sheet type. In the previous subsections we analytically determined approximate relationships for the axial resolution. A more accurate estimate can be obtained numerically by calculating the vectorial point spread function for all beam types and integrating its intensity along the  $y$ -axis. **Fig. 2d** shows the axial resolution as a function of numerical aperture (NA) for the four light sheet types considered here. It can be seen that for all types of light sheet, the smallest features can be resolved at the highest NA. Diffraction-limited resolution is achieved by the apertured Gaussian light sheet (grey dotted line). At the NA used in our experiments, 0.42, this corresponds to 726 nm. The Bessel light sheets employed, Bessel10 (solid blue line) and Bessel5 (red dashed line), can achieve potentially an axial resolution of 1.9  $\mu\text{m}$  and 3.9  $\mu\text{m}$ , respectively. Although the practical field-of-view of the Airy beam (solid green line) is larger than that of both Bessel beams, we find an axial resolution of 865 nm for the Airy light sheet, considerably below that of the Bessel light sheets.

## Supplementary Note 4: Experimental comparison of the photobleaching rate

We investigate the impact of irradiation experimentally by time-lapse measurement of the fluorescence while repeatedly scanning a sample volume with the different light sheet types. As the Bessel beam light sheets can only be created by digitally scanning a focused beam, we used this technique for all light sheet types. Instead of scanning a focused beam, the Airy and Gaussian light sheets can in principle be created using a cylindrical lens, thus reducing the peak irradiance. We kept the total illumination power constant at  $0.7\text{ mW}$  throughout the experiment in order to accelerate the bleaching of homogeneous test samples with a high concentration of Cy3-streptavidin in polyacrylamide gel (see Online Methods).

<i>Light Sheet Type</i>	<i>BR (scan<sup>-1</sup>)</i>	<i>BR 95% CI (scan<sup>-1</sup>)</i>	<i>HL (scan)</i>	<i>HL 95% CI (scan)</i>
Gaussian, major term (77%)	$0.76 \pm 0.05$	$0.66 \rightarrow 0.86$	0.9	$0.8 \rightarrow 1.1$
Gaussian, minor term (23%)	$0.068 \pm 0.007$	$0.054 \rightarrow 0.082$	10.1	$8.4 \rightarrow 12.7$
Bessel10	$0.045 \pm 0.002$	$0.041 \rightarrow 0.049$	15.4	$14.1 \rightarrow 16.9$
Bessel5	$0.034 \pm 0.002$	$0.031 \rightarrow 0.038$	20.2	$18.5 \rightarrow 22.4$
Airy	$0.030 \pm 0.001$	$0.028 \rightarrow 0.033$	22.8	$21.1 \rightarrow 24.8$

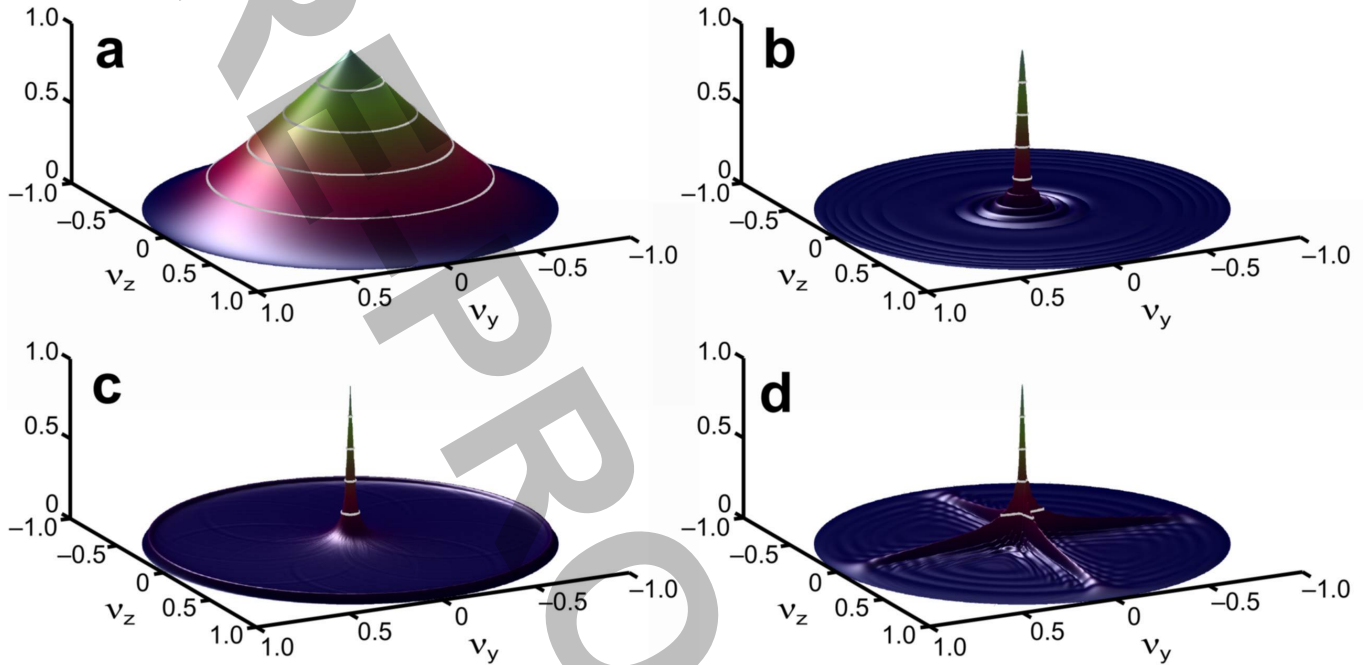
**Supplementary Table S2.** Comparison of the bleaching rates for various digitally scanned light sheet types. For each type of light sheet, we monitored the fluorescence while performing 100 light sheet scans. The obtained fluorescence intensity curve was well fitted by an exponential model in case of the Bessel and Airy beams. A bi-exponential model was required for the apertured Gaussian light sheet to achieve comparable fitting. The bleaching process of the Gaussian light sheet has a dominant (77%) term with the high rate, and a less important slower rate term. Both rates are significantly higher than those of the propagation-invariant light sheet types. The bleaching rate (BR), the corresponding 95% two-sided confidence intervals (CI), the fluorescence half life (HL), as well as the 95% confidence intervals are shown for all exponents.

It can be seen from **Supplementary Table S2** that the apertured Gaussian light sheet causes the highest rate of photobleaching, followed by the Bessel10, while the Bessel5 and Airy light sheets show the lowest rates of photobleaching. Even though the peak power of the Airy light sheet is slightly higher than that of Bessel5, the peak power of that scanned Bessel beam used to create the light sheet is approximately 5 times higher than that of the Airy beam. Although peak power is not the only factor to consider in photobleaching, it appears that in practice the scanned Airy beam light sheet achieves comparably low levels of bleaching as the Bessel5 light sheet. Note however that Bessel5 cannot achieve a wide field-of-view with high resolution unless hybrid techniques are used that require at least three irradiations per plane. Selective detection of fluorescence to increase the axial resolution does reduce the useful signal. This could be compensated by longer integration times and thus samples exposure. Although the Airy light sheet does not require selective detection, only approximately 74.3% of the fluorescence is emitted within the depth-of-field of the detection objective. However, such signal reduction does not offset the 25-fold difference in dominant bleaching rate. Furthermore techniques to extend the depth-of-field could be considered to improve the efficiency if required<sup>26</sup>.



## Supplementary Note 5: Modulation transfer function of a light sheet

The modulation transfer function (MTF) of the light sheet is defined as the absolute value of its normalized optical transfer function. The optical transfer function of a light sheet is defined here as the  $z$ -axis Fourier transform of its intensity. As the single photon light sheet is created by time-averaging of a focused beam along the  $y$ -axis, it follows that the MTF of the light sheet is simply an axial section through the origin of the transfer function of the focused beam, calculated from the two-dimensional ( $y-z$ ) Fourier transform. Only for the Airy beam a rotational asymmetry is seen (**Supplementary Fig. S2**). Preferential orientations of the focused beam in the  $y-z$  plane may thus exist.

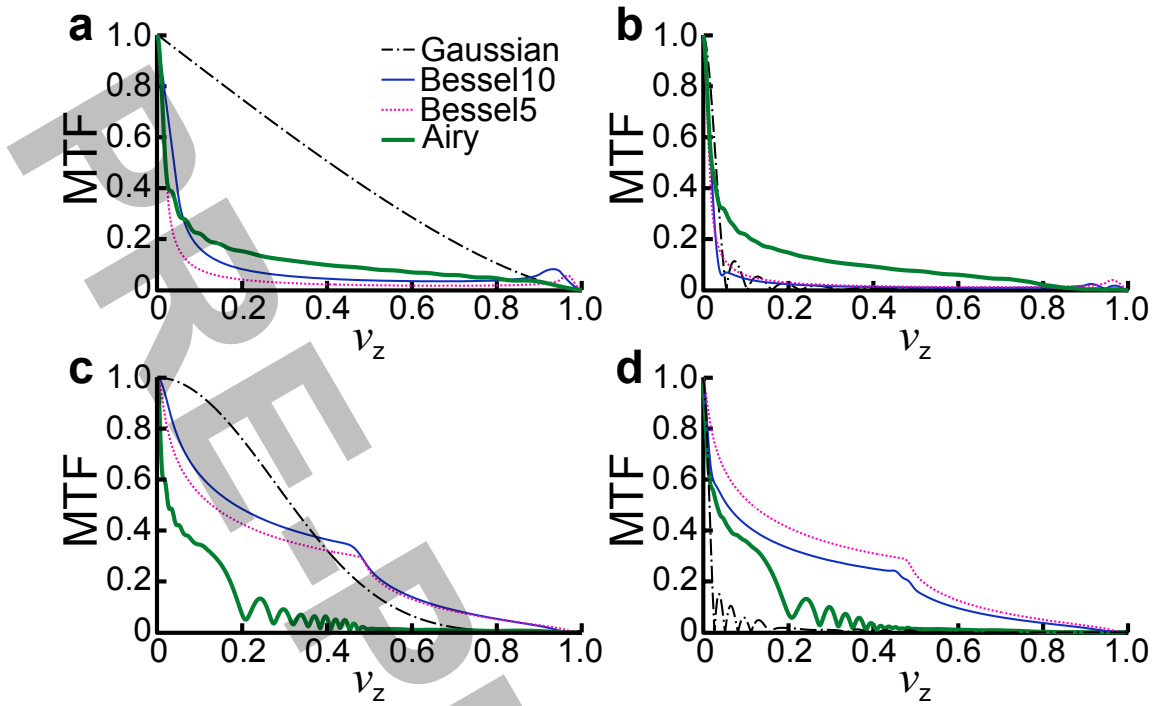


**Supplementary Figure S2.** The two-dimensional modulation transfer function of various beam types used for the creation of a light sheet. (a) The beam MTF of an apertured Gaussian at its waist and (b) at a plane  $25\ \mu\text{m}$  beyond the waist. (c-d) The beam MTFs of the propagation invariant Bessel5 and Airy beams, respectively. The  $z$ -axis sections, relevant to light sheet microscopy, at the light sheet waist and at  $25\ \mu\text{m}$  are shown in **Fig. 1e** and **f**, respectively.

Upon propagation along the  $x$ -axis, the intensity profile of the Airy beam translates laterally along the diagonal axis  $y \equiv z$  to follow a curved trajectory. In principle the Airy beam could be rotated by  $45^\circ$  around its propagation axis,  $x$ , so that its curvature lies in the plane of the light sheet ( $x-y$ ), effectively creating a planar light sheet with the curved beam. Such a rotation would not alter the propagation invariance and ‘self-healing’ properties; however, it may alter the imaging contrast and it raises the question of what orientation of the cubic phase modulation yields the highest contrast.

We can determine the most practical choice by considering the two-dimensional MTF of the ‘focused’ Airy beam. As seen in **Supplementary Fig. S2d**, the high contrast sections through the origin of the MTF are both aligned with the Cartesian system axes. The initially proposed orientation would thus achieve high contrast. On the other hand, the low values observed on the diagonal indicate that a mask rotation of  $45^\circ$ , thus maintaining the propagation path within the light sheet plane, should be avoided because it would lead to low contrast.

While the single-photon modulation transfer function (MTF) can be calculated as the normalized absolute value of the autocorrelation of the pupil function, the two-photon MTF can be calculated via the autoconvolution of the single-photon optical transfer function itself. The single-photon MTFs depicted in **Supplementary Fig. S3a** and **b** show that the Airy beam MTF is significantly higher than that of the Bessel beam, one could conclude that the Airy beam would therefore also yield higher two-photon contrast. In fact the contrary is true, as is seen in **Supplementary Fig. S3c** and **d**. Due to the asymmetry of the Airy beam, its single-photon optical transfer function is not strictly real valued, giving rise to the zeros seen in its autoconvolution and thus two-photon MTF. In contrast, the single-photon optical transfer function associated with the Bessel beam illumination is strictly real and positive, and its autoconvolution integral yields the high values for the two-photon transfer function seen in **Supplementary Fig. S3c** and **d**. Notice that the contrast at mid-to-high spatial frequencies is actually higher than that at the waist



**Supplementary Figure S3.** Modulation transfer functions for the four light sheets using single and two-photon excitation. Plots are shown for the light sheet at its waist (a,c), and at 25  $\mu\text{m}$  (c,d), for single-photon excitation (a,b), and for two-photon excitation (c,d). The spatial frequency ( $\nu_z$ ), is normalized to the highest transmitted spatial frequency:  $2NA/\lambda$ , where  $\lambda$  and  $NA$  are, respectively, the illumination wavelength and the numerical aperture.

of the apertured Gaussian light sheet. This is convenient as the SNR typically decreases with spatial frequency and will therefore be most critical for the mid-to-high spatial frequencies. By keeping the power constant, yet illuminating the sample only with the larger k-vectors, two-photon Bessel beam illumination can improve contrast and the practically achievable resolution. We can therefore conclude that the Airy beam is preferred over the Bessel beam in single-photon excitation and the situation is *vice versa* for two-photon experiments.

## Supplementary Note 6: Description of the deconvolution algorithm.

Raw images recorded with an Airy light sheet microscope have a characteristic blur in the axial dimension,  $z$ . The distinctive mark of the asymmetric transversal structure of the Airy light sheet is clearly visible in the recorded microsphere image (**Fig. 2c**). This can be understood as the fluorescence emitted by each microsphere is directly related to its position within the light sheet. Due to the propagation invariance of the Airy beam the shape of the asymmetric blur is relatively independent of the position in the field-of-view. The detected image stack can be approximated as a convolution of the fluorophore distribution in the sample with the light sheet intensity distribution, thus enabling standard deconvolution techniques to recover the axial resolution across the field-of-view.

The recorded three-dimensional data stacks are processed using a standard minimum mean square error (Wiener) filter applied to the axial dimension. A general description of this filter, its rationale, as well as examples can be found in<sup>20</sup> (3<sup>rd</sup> edn., Section 5.8: “Minimum Mean Square Error (Wiener) Filtering”, pp 374–379). In principle a deconvolution operation could be implemented as a numerical convolution with a ‘filtering’ kernel in real space. However, in reciprocal space the convolution operation becomes a regular multiplication, which is often more efficient to implement. Our implementation follows this approach.

In reciprocal space, the fluorophore distribution is represented as a set of independent Fourier components. The convolution acts on each spatial frequency component independently as a multiplication with the corresponding value of the optical transfer function,  $H(x, \nu_z)$ . The deconvolution corrects the components of the recorded image stack,  $I(x, y, \nu_z)$ , by multiplication with the Wiener filter,  $H_W(x, \nu_z)$ . The filter values are determined so to minimize the expected mean square error for a signal-to-noise model,  $SNR(\nu_z)$ , and is given by the equation:

$$H_W(x, \nu_z) = \frac{H(x, \nu_z)^*}{|H(x, \nu_z)|^2 + SNR(\nu_z)^{-2}}, \quad (22)$$

where \* indicates the complex conjugate.

Note that digital post-processing is often hampered by a limited knowledge of the optical transfer function. This can give rise to an image shift and ‘ringing’ artifacts when the distance to the focal plane of the Airy beam is uncertain<sup>27</sup>. However, this is not an issue in light sheet microscopy since, due to the orthogonal detection, a direct relationship exists between the propagation of the light sheet and the position on the detector array. Propagation invariance is thus not strictly necessary for extending the field-of-view of light sheet microscopy, and the optical transfer function can be written as:  $H(x, \nu_z)$ , a function of both the real coordinate  $x$  and the reciprocal coordinate  $\nu_z$ . As long as the optical transfer function has significant values at all relevant spatial frequencies, linear deconvolution can accurately correct for both the amplitude and phase change. This effectively cancels the image warping due to the curvature of the Airy beam light sheet as well as any residual phase artifacts originating from the finite aperture used to generate the Airy beam.

The implementation of the deconvolution algorithm can be separated into two main parts: the calculation of the filter, and the application of the filter to the recorded data. We discuss these separately in the following two subsections.

### Calculation of the deconvolution filter

This first phase of the algorithm can take up to several minutes to compute on a modern desktop computer; however, once a filter is calculated for each excitation wavelength, it can be reused for all data recorded with that microscope configuration (numerical aperture, beam type, voxel size, ...).

1. Calculate the  $x - z$  intensity profile of the light sheet in the sample volume.
  - (a) Determine the intensity distribution,  $PSF(x, y, z)$ , of focused, unit-total-intensity, beam used to generate the light sheet by digital scanning. The intensity distribution must be determined at the  $x$  coordinates that geometrically project to the detector pixel columns and at  $z$  the coordinates corresponding to the zero-centered stage positions. A coarser, Nyquist, spacing is used for the  $y$  coordinates to minimize the calculation time and memory requirements. For simplicity of notation and generality, in what follows we use the mathematical operations using functions such as  $PSF(x, y, z)$ , independently of the chosen sample coordinates.
  - (b) Integrate the intensity along the  $y$ -axis:  $LS(x, z) = \int_{-\infty}^{+\infty} PSF(x, y, z) dy$ .
2. Calculate the light sheet OTF,  $H(x, \nu_z)$ , as the one dimensional Fourier transform in  $z$  of the light sheet intensity distribution:  $H(x, \nu_z) = \mathcal{F}_z\{LS(x, z)\}$ , where  $\nu_z$  is the spatial frequency in the axial dimension. To

prevent edge artefacts in the deconvolution, the light sheet is first zero-padded in  $z$  to double its size in the axial dimension, before calculating the discrete Fourier transform.

3. Model the signal-to-noise ratio as a power law distribution:

(a) Calculate the signal-to-noise ratio as a function of spatial frequency,  $\nu_z$ :  $SNR(\nu_z) = k\nu_{\text{cut-off}}/\nu_z$ , where  $k$  is a filter constant adjusted for the signal-to-noise of the recorded data, and  $\nu_{\text{cut-off}}$  is the maximum spatial frequency transmitted by the illumination path. This spatial frequency is given by  $2NA/\lambda$ , where  $NA$  is the effective numerical aperture and  $\lambda$  is the wavelength of the excitation.

4. Calculate the Wiener filter as:  $H_W(x, \nu_z) = H(x, \nu_z)^* / (|H(x, \nu_z)|^2 + SNR(\nu_z)^{-2})$ , where  $*$  designates the complex conjugate. Note the singularity at  $SNR(0)$  is not an issue as the term is elevated to a negative power. Division by zero can thus be avoided by working directly with the inverse of the signal-to-noise ratio.

In case of multi-color fluorescence imaging, one filter is calculated per color channel.

## Deconvolution of the recorded data sets

Once the deconvolution filter is determined for each color channel, it can be applied to the recorded data per channel,  $i_{\text{rec}}(x, y, z)$ , as follows:

1. To minimize potential deconvolution artefacts at the start and end of the data set, replicate the first and last frame of the image stack so to double the axial dimension of the data cube. We represent the extended data set with the discrete function  $i_{\text{ext}}(x, y, z)$ .
2. If required, use cubic interpolation of the images to correct for coordinate errors due to imperfect axial-translation. We determined a lateral drift of 2.5% by imaging fluorescent microspheres.
3. Calculate  $I(x, y, \nu_z) = \mathcal{F}_z \{i_{\text{ext}}(x, y, z)\}$ , the one-dimensional Fourier transform along the  $z$ -axis of the extended image stack.
4. Calculate the deconvolved volumetric image,  $i_{\text{dec}}(x, y, z)$ , as the inverse Fourier transform in  $\nu_z$  of  $I_{\text{dec}}(x, y, \nu_z)$ , the product of  $I(x, y, \nu_z)$  with the earlier calculated Wiener filter:  $i_{\text{dec}}(x, y, z) = \mathcal{F}_{\nu_z}^{-1} \{I(x, y, \nu_z) \cdot H_W(x, \nu_z)\}$ .
5. Remove the edge-extension by cropping the resulting image to half its size in the axial dimension.

The discrete functions in real space coordinates,  $(x, y, z)$ , are readily represented in computer memory as three-dimensional matrices. The largest data set is the matrix of recorded data, extended to twice its size in the axial dimension. The light sheet and Wiener filter are independent of the  $y$  coordinate and can thus be stored compactly as two-dimensional matrices.

The Fourier transform of a discrete function is not necessarily discrete; however, in this case it is the sinc-interpolant of a discrete function. The values of the latter are given by the discrete Fourier transform, implemented efficiently using the fast Fourier transform algorithm. The data in frequency space can be stored in two or three-dimensional matrices of size equal to their respective real-space equivalents. The values at the discrete coordinates are sufficient to calculate the inverse Fourier transform at the initial real space coordinates.

## Supplementary References

---

18. Fahrbach, F. O. & Rohrbach, A. *Nat. Commun.* **3**, 632 (2012).
19. Gustafsson, M. G. *J. Microsc.* **198**, 82–87 (2000).
20. Gonzalez, R. C. & Woods, R. E. *Digital Image Processing* (Prentice Hall, 2007), third edition edn.
21. Berry, M. V. & Balazs, N. L. *Am. J. Phys.* **47**, 264–267 (1979).
22. Polynkin, P., Kolesik, M., Moloney, J. V., Siviloglou, G. A. & Christodoulides, D. N. *Science* **324**, 229–232 (2009).
23. Ellenbogen, T., Voloch-Bloch, N., Ganany-Padowicz, A. & Arie, A. *Nature Photon.* **3**, 395–398 (2009).
24. Porat, G., Dolev, I., Barlev, O. & Arie, A. *Opt. Lett.* **36**, 4119–4121 (2011).
25. Goodman, J. W. *Introduction to Fourier Optics* (Roberts & Company Publishers, 2005), 3rd edn.
26. Dowski, E. R. & Cathey, W. T. *Appl. Opt.* **34**, 1859–1866 (1995).
27. Demenikov, M. & Harvey, A. R. *Opt. Express* **18**, 8207–8212 (2010).